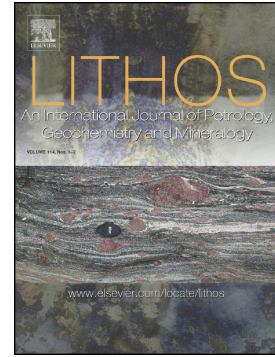


Accepted Manuscript

Petrogenesis of the late Miocene Combia Volcanic complex, northwestern Colombian Andes: Tectonic implication of short term and compositionally heterogeneous arc magmatism

J.S. Jaramillo, A. Cardona, G. Monsalve, V. Valencia, S. León



PII: S0024-4937(19)30087-8
DOI: <https://doi.org/10.1016/j.lithos.2019.02.017>
Reference: LITHOS 4985
To appear in: *LITHOS*
Received date: 2 October 2018
Accepted date: 19 February 2019

Please cite this article as: J.S. Jaramillo, A. Cardona, G. Monsalve, et al., Petrogenesis of the late Miocene Combia Volcanic complex, northwestern Colombian Andes: Tectonic implication of short term and compositionally heterogeneous arc magmatism, *LITHOS*, <https://doi.org/10.1016/j.lithos.2019.02.017>

This is a PDF file of an unedited manuscript that has been accepted for publication. As a service to our customers we are providing this early version of the manuscript. The manuscript will undergo copyediting, typesetting, and review of the resulting proof before it is published in its final form. Please note that during the production process errors may be discovered which could affect the content, and all legal disclaimers that apply to the journal pertain.

Petrogenesis of the Late Miocene Combia Volcanic Complex, northwestern Colombian Andes: Tectonic implication of short term and compositionally heterogeneous arc magmatism.

Jaramillo, J.S.^{1,2}, Cardona, A.^{2,3}, Monsalve, G.^{2,4}, Valencia, V.⁵, León, S.^{2,6,7}

¹Departamento de Materiales y Minerales, Universidad Nacional de Colombia, Medellín, Colombia.

²Grupo de Investigación en Geología y Geofísica (EGEO), Universidad Nacional de Colombia, Medellín, Colombia.

³Departamento de Procesos y Energía, Universidad Nacional de Colombia, Medellín, Colombia.

⁴Universidad Nacional de Colombia, Departamento de Geociencias y Medio Ambiente, Medellín, Colombia.

⁵School of Earth and Environmental Science, Washington State University, Pullman, USA.

⁶Departamento de Geociencias, Universidad Nacional de Colombia, Bogotá, Colombia.

⁷Smithsonian Tropical Research Institute, Balboa, Ancon, Republic of Panama.

Abstract

During the Miocene, the evolution of the Northern Andes was influenced by the subduction of the young Oceanic Nazca Plate and the final collision of the Panama-Chocó Block (PCB) with the continental margin of Colombia. This work presents an integrated field, geochemical, Hf-Nd-Sr isotopic and geochronological study of volcanic arc front rocks of the Combia volcanic complex in the northern segment of the Cauca-Valley (North of 5°N) in order to reconstruct the petrologic and tectonic significance of a short life arc with a very heterogeneous geochemical signature. The Combia volcanic complex includes a series of basalts, andesites, pyroclastic rocks, porphyritic andesitic-dacitic domes, and dacitic to andesitic porphyries, with zircon U-Pb crystallization ages between 8.5 to 5.2 Ma. Negative anomalies of Nb and Ti, enrichment in Light Rare Earth Elements (LREE) and depletion in Heavy Rare Earth Elements (HREE) are characteristic of magma origin in a convergent

margin setting. This magmatism shows different tholeiitic, calc-alkaline, and adakite-like geochemical signatures, which may be related to an initial adiabatic-controlled dry melting, followed by wet melting conditions from the hydrated mantle wedge. Variations in crustal thickness between 17 - 45 km estimated by the Ce/Y, La/Yb, and Sr/Y ratios are related to local thinning of a previously thickened continental crust. Such pattern can be explained by strain partitioning in which crustal thinning may be a relatively local phenomenon. Arc magmatism in this segment of the margin apparently migrates eastward from the Western Cordillera to the Cauca-Valley between 11-9 Ma and was followed by a magmatic quiescence after ~5.2 Ma. This spatio-temporal history is consistent with continuous oblique convergence of the Nazca Plate and slab flattening beneath the continental margin until it achieves its modern tectonic configuration.

1. Introduction

Magmatic arcs are influenced by the characteristics of both the upper and lower plates including plate convergence rates, subduction angle, upper plate structural history and thickness, among other variables. The compositional variations of magmatism trace such changes, and together with its spatial distribution have become a cornerstone for the understanding of the long term evolution of the Andean margin during the Cenozoic (Haschke et al., 2006; Kay et al., 2005).

After the Farallon plate fragmentation at ca. 23 Ma (Lonsdale, 2005), the formation of the oceanic Nazca plate and its interaction with the South American plate, together with the collision of the Panamá-Chocó Block (PCB), were responsible for the growth of the Northern Andean magmatic arc and orogenic build-up (Duque-Caro, 1990; León et al., 2018; Mora et al., 2013; Parra et al., 2009).

The Miocene magmatic arc north of 5°N along the Colombian Andes records the volcanic arc reactivation after a Late Paleogene magmatic gap (Bayona et al., 2012). This magmatism was associated with different pull-apart basins (MacDonald et al., 1996), which are inherited from structures created during the Late Cretaceous and Middle Miocene collisional events (Jaramillo et al., 2017; León et al., 2018; Montes et al., 2015; **Figure 1**). .

In this contribution zircon U-Pb crystallization ages, whole rock geochemistry, and Hf-Sr-Nd isotopes on basalts, andesites and pyroclastic rocks related to the Combia volcanic complex, are integrated in order to understand the processes that controlled the growth of

the Miocene magmatic arc and its relation with Northern Andean tectonics. The new results, when integrated with published constraints, show that the Miocene magmatism north of 5°N extends from 13 to 5.2 Ma, and is characterized by an early phase that includes alkaline basalts, followed by a highly heterogeneous record including tholeiitic to calc-alkaline series and adakite-like signatures. The short life and compositionally heterogeneous nature of this magmatic arc is considered characteristic of continental margins with transtension/transpression and structural inheritance.

2. Geological Framework

The tectonic configuration of the continental margin of Colombia is characterized by the oblique subduction of the Nazca plate underneath South America at a rate of about 53-58 mm/yr (Mora-Paez et al., 2019; Trenkamp et al., 2002, **Figure 1**) that followed previous changes in the angle, direction and convergence rates during the Oligocene-Miocene (Chiarabba et al., 2016; Echeverri et al., 2015; Somoza, 1998; Wagner et al., 2017). The modern active magmatic arc is mainly expressed approximately south of 5.5°N, and is characterized by andesitic lava flows and pyroclastic rocks with a prominent calc-alkaline signature and minor adakite-like products (Calvache and Williams, 1998; Toro-Toro et al., 2008).

Vargas and Mann (2013) proposed the existence of two different subduction segments north and south of ca 5.5°N, which were related to flat and normal dip subduction (~ 35°) respectively (Chiarabba et al., 2016; Ojeda and Havskov, 2001; Wagner et al., 2017). This tectonic setting followed the ca. 23 Ma partition of the Farallon Plate and the subsequent formation of the Cocos and Nazca plates with their associated aseismic ridges (Lonsdale, 2005) subducting underneath the South and Central American margins. The limit between these two subduction segments coincides with an extinct oceanic ridge within the Nazca plate (Sandra Ridge), that has been subducting under the South American continent during most of the Neogene (Lonsdale, 2005), and migrated from a southern position (Morell, 2015).

The history of this complex tectonic scenario is recorded in different hinterland basins influenced by strike slip tectonics, such as in the Cauca-Patia and Amagá Basins (Silva-Tamayo et al., 2008, **Figure 1**); in the exhumation patterns of the Colombian cordilleras (León et al., 2018; Mora et al., 2013; Parra et al., 2009); in the evolution of the foreland basins, that record major exhumation pulses at ca. 15 - 10 and 6 - 3 Ma (Mora et al., 2013;

Parra et al., 2009); and especially in the spatial distribution and compositional characteristics of Miocene arc related rocks (Aspden et al., 1987; Echeverri et al., 2015; Leal-Mejía, 2011).

3. Miocene-Pliocene magmatic and sedimentary record north of 5.5°N

The spatio-temporal evolution of the Mio-Pliocene magmatic record in the Colombian margin, including the Combia volcanic complex, is characterized by an initial eastward migration of the magmatic front during the Miocene until its apparent extinction north of 5.5°N (**Figure 1**), which may be mainly related to changes in the subduction angle (Wagner et al., 2017). North of 5°N, the magmatic and structural evolution records the oblique subduction of a young Miocene Nazca plate since the Early Miocene (Somoza, 1998) that caused strain partitioning associated with extensional tectonics in pull-apart like systems. This magmatism, which may have started in a western position by 13 Ma (Zapata and Rodríguez, 2011), migrates eastward by middle Miocene (Toussaint, 1996), recording the re-organization of the continental margin after the PCB collision with western South America (León et al., 2018; Montes et al., 2015). Structural relations demonstrate that several post Oligocene and late Miocene deformational events have affected the Miocene-Pliocene basins, including the Combia volcanic complex, until arc magmatism finally was absent north of ca. 5.5°N (Wagner et al., 2017).

Oligocene to Pliocene sedimentary and magmatic rocks are exposed between the western and eastern flanks of the Central and Western Cordilleras along the Cauca Valley depression (**Figure 1, 2A,B**). Siliciclastic rocks of Oligo-Miocene age are included within the N-S elongated Amagá Formation of pull-apart origin, cut by several regional faults of the Romeral Fault System, which documents a long-time series of re-activation tectonics since the Late Cretaceous, with a significant strike-slip component (MacDonald et al., 1996; Sierra et al., 2012). This unit includes interlayered conglomerates, sandstones, mudstones, and coal beds, interpreted to have accumulated in braided and meandering fluvial environments (Silva-Tamayo et al., 2008). An angular unconformity separates this sequence from the overlying Combia volcanic complex that is also associated with porphyritic bodies (Grosse, 1926, **Figure 2C**). The Combia volcanic complex, which is also located within this deformational system, is characterized by a sequence of volcano-sedimentary rocks including basalts, andesites, porphyries, agglomerates, tuffs, sandstones, siltstones, and conglomerates, and plutonic rocks such as tonalities, granites and granodiorites. Published K-Ar, Ar-Ar, and U-Pb ages have shown that the magmatism south of 5°N, occurred between

ca. 11.8 and 4.7 Ma (Bissig et al., 2017; Leal-Mejía, 2011; Naranjo et al., 2018), and the volcanic materials have shown different calc-alkaline and adakite-like geochemical signatures; whereas to the north, the Combia volcanic complex has ages between ca 9 Ma and 5.2 Ma and includes different tholeiitic, calc-alkaline and adakite-like compositional signatures which have been related to a model of arc maturation (Leal-Mejia, 2011; Tejada et al., 2007).

The siliciclastic rocks of the Combia volcanic complex are characterized by tabular-shaped layers of poorly sorted conglomerates, and immature sandstones and mudstones, that have been associated to continental debris flows and braided river environments in the late Miocene, associated to the formation of different volcanic edifices (Ramirez et al., 2006 and references therein).

4. Methods

4.1 Field geology and petrography

Field work was carried out in the Cauca depression and the western flank of the Central Cordillera, near the towns of Fredonia, Venecia, and La Pintada (**Figure 2A,B**). Volcanic, sedimentary and plutonic rocks associated to the Combia volcanic complex were described in 160 field stations. Relatively fresh samples were collected from tuffs, agglomerates, andesites, basalts, andesitic-dacitic domes and intrusive porphyritic rocks for petrography, geochemical and isotopic analyses. Thirty-nine thin sections were analyzed by point counting. For the pyroclastic particles we followed Fisher and Schmincke (1984) terminology, with "*Juvenile*" related to fragments derived directly from the erupting magma, "*accessory*" for fragments that are from co-magmatic volcanic rocks derived from previous volcanic eruptions, and "*accidental*" to those derived from the basement which may have any composition. In order to review the spatio-temporal distribution of magmatic rocks from the Miocene to current Colombian arcs, we have compiled ~ 230 published igneous ages. Only U-Pb, K-Ar, and Ar-Ar ages were included in this compilation; Rb-Sr and fission track ages were discarded because of the high element mobility and their relation with low temperature cooling. Zircon U-Pb ages were preferred over K-Ar and Ar-Ar for single samples, whereas in the case of the Ar system the highest closure temperature age was preferred. We finally obtained a geo-referenced database of ca 150 ages.

4.2 LA-ICP-MS zircon geochronology

Zircon concentrates from seven samples were obtained at the Zirchron Llc Company, by rough-crushing, pulverizing, and finally, sieving in disposable 330 μ m mesh. This fraction was passed through a water table (Wilfley®) and followed by magnetic separation using a Frantz ® isodynamic separator. Methylene iodide (3.3 g/cm³) was used to further concentrate the zircon crystals. Zircons were subsequently handpicked under the microscope and mounted in an epoxy puck along with the Plešovice, 91500, Temora, and MUNzirc standards and finally polished to expose crystal faces.

The LA-ICP-MS U-Pb zircon analysis was carried out at the Radiogenic Isotope and Geochronology Lab (RIGL) at Washington State University in Pullman, USA. Analyses were done using a New Wave 213 nm solid state (Nd:YAG) laser ablation system couple to a ThermoFinnigan Element2 ICPMS, following the protocol described in detail by Chang et al. (2006). Analyses of unknown zircons and quality control zircons are interspersed with analyses of external calibration standards, typically with 10 unknowns bracketed by multiple analyses of two different zircon standards (Plešovice and 91500). To calibrate the ²⁰⁶Pb/²³⁸U and ²⁰⁷Pb/²³⁵U ages the Plešovice zircon standard was used (337Ma; Sláma et al., 2008). The concentrations of U, Th, Pb are estimated using the analyses of 91500 zircon, the common Pb correction was carried out by the Williams (1998) method, and the uranium-lead data ages were calculated using Isoplot (Ludwig, 2012). For magmatic ages, the error is propagated with the analytical and systematical error and are calculated to 2 σ . The geochronological data are presented in the Supplementary data 1.

During the present study, zircon Plešovice standard yield a weighed mean ²⁰⁶Pb/²³⁸U age of 336.5 \pm 2.5 Ma (n= 16) (compared to an ID-TIMS age of 337Ma; Sláma et al., 2008) and the Temora zircon yields a weighted mean age for ²⁰⁶Pb/²³⁸U of 417.9 \pm 5.4 Ma (n= 5) (compared to a CA-ID- TIMS age of 416.78 \pm 0.33 Ma; Black et al., 2004).

4.3 Geochemistry

Whole rock geochemical analysis of 24 samples was conducted on igneous rocks from the Combia volcanic complex; representative data of 8 samples are reported in Table 1 and all samples are presented in Supplementary data 2. The analyzed samples include 9 basalts, 5 andesites, 6 explosive rocks (i.e., agglomerates, tuffs, and vitrophyre), 3 andesitic and dacitic porphyry samples, and a single gabbroic dyke. The samples were crushed using a jaw crusher and powdered using a tungsten carbide ring mill. Both X-ray fluorescence (XRF) and inductively coupled plasma-mass spectrometry (ICP-MS)

analyses were conducted in the Peter Hooper GeoAnalytical Lab of Washington State University, following analytical procedures described in Johnson et al. (1999). The Geochemical data were handled and processed using the GCDkit free software (Janoušek et al., 2006).

4.4 Lu-Hf Isotopes in zircon

The zircon Lu-Hf isotopic composition was determined for crystals analyzed by U-Pb geochronology from two tuffs, one porphyry, one andesitic dome, and one lahar sample. Isotopic analyses were also determined at the RIGL using a ThermoFinnigan Neptune mass spectrometer coupled to a New Wave 213 nm Nd:YAG laser, using a spot size of 40 μm , a laser fluence of $\sim 7 \text{ J/cm}^2$, and a repetition rate of 10 Hz. This study used the same instrument configuration, operating parameters, and data reduction methods outlined by Fisher et al. (2014), with the exception that U-Pb ages were not simultaneously determined. Data reduction was performed using the scheme of the IOLITE software package.

Over the course of this study, secondary standard analyses included 8 analyses of the MUNzirc4 ($^{176}\text{Hf}/^{177}\text{Hf} = 0.282135 \pm 7$, Fisher et al., 2011), which yielded a $^{176}\text{Hf}/^{177}\text{Hf}$ of 0.282124 ± 23 (2σ). Analyses of these quality control zircons agree well with published S-MC-ICPMS isotope compositions of purified Hf from these zircons, attesting to the accuracy of the interference correction methods employed.

Present day ϵHf values were calculated using the CHUR parameters reported by Bouvier et al. (2008); the depleted mantle Hf evolution curve was calculated from present-day depleted mantle values of $^{176}\text{Hf}/^{177}\text{Hf}$ DM(0) = 0.283240 and $^{176}\text{Lu}/^{177}\text{Hf}$ DM(0) = 0.03979 (Vervoort et al., 2015). Laser ϵHf values are reported with 2σ uncertainty in Supplementary data 3.

4.5 Whole rock Sr-Nd Isotopes

Whole-rock Sr and Nd isotope composition of one gabbro, one basalt, two andesites and one andesitic porphyry from the Combia volcanic complex were acquired at the RIGL using the Thermo-Finnigan Neptune multicollector system. Results are presented in Table 2. After crushing the samples, they were powdered using an agate mill jar and balls. The procedures for Sr and Nd isotopes preparation are the same as those in Gaschnig et al. (2011). The Sr

analyses were corrected for mass fractionation using $^{86}\text{Sr}/^{88}\text{Sr} = 0.1194$ and normalized using NBS-987. The average reproducibility, with two standard deviations of $^{87}\text{Sr}/^{86}\text{Sr}$, was ± 0.00005 . The initial isotopic values were calculated using Rb and Sr concentrations from the XRF. The Sm and Nd isotope analyses followed the procedures described in Vervoort and Blichert-Toft (1999). Sm mass fractionation was corrected using $^{147}\text{Sm}/^{152}\text{Sm} = 0.56081$, and Nd was corrected for mass fractionation using $^{146}\text{Nd}/^{144}\text{Nd} = 0.7219$ and normalized using the Ames Nd standard (± 0.000020 2σ average reproducibility). The ϵNd values were calculated using present day values of $^{143}\text{Nd}/^{144}\text{Nd} = 0.512630$ and $^{147}\text{Sm}/^{144}\text{Nd} = 0.1960$ for CHUR (Bouvier et al., 2008).

5. Results

5.1 Field relationships and petrography

Field work was carried out between the Central and Western Cordilleras of Colombia, in the Cauca River depression, along two different zones between $5^{\circ}20'$ and $6^{\circ}11'$ N. A northern zone that is near the towns of Fredonia and Venecia, and a southern zone between La Pintada and La Felisa towns (**Figure 2A,B**). The studied volcano-plutonic units of the Combia volcanic complex are characterized by discordant and intrusive relations with folded fluvial siliciclastic rocks of the Oligocene to middle Miocene Amagá Formation. Volcanic rocks include intercalated basalts, andesites, tuffs, block or breccia tuff (agglomerates). A series of andesite dykes together with andesitic and dacitic porphyries intrude the volcanic rocks. Additionally, some domes of andesitic to dacitic composition are also observed intruding sedimentary and volcanic rocks from the Combia volcanic complex (**Figure 2C**).

Stratified rocks of the Combia volcanic complex are faulted near major regional faults, but they are also characterized by symmetric synclinal folds with flanks dipping around $10 - 20^{\circ}$ and an interlimb separation around 125° ; whereas the underlying Amagá Formation is characterized by symmetric synclinal folds with flanks dipping around $22-40^{\circ}$ and an interlimb separation around 100° , which represent at least two different deformation stages.

5.1.1 Basaltic flows

Basalts crop out at both flanks of the Cauca River. These rocks include vesicles and subhedral to euhedral plagioclase phenocrysts up to 0.8 cm (**Figure 3A**) and show microcrystalline, intersertal, intergranular, and subophitic textures, while glomeroporphyritic

plagioclases are observed less frequently (**Figure 3B**). The average modal composition of basalts is characterized by plagioclase between 9 and 40% (An₈₂-An₅₈), clinopyroxene (augite) between 27 and 58%, and olivine between 1 and 11%. Epidote, chlorite, and biotite were formed after the alteration of plagioclase and pyroxene. These basalts may vary to porphyritic texture characterized by augite phenocrysts up to 1.2 cm in size and some plagioclases up to 3 mm, which are embedded in a plagioclase and augite matrix. Pyroxene and plagioclase are characterized by a matrix with curved boundaries, which are characteristic of flow textures (**Figure 3C,D**). These basalts are intruded by coarse-grained gabbroic sills with a thickness between 2 and 50 cm. Gabbros contain ~56% plagioclase, 29% augite, 3% quartz, and ~4% of chlorite formed after pyroxene; titanite (1%) is the main accessory mineral. These rocks are overlain by interlayered pyroclastic, basaltic, and andesitic rocks.

5.1.2 Andesites

Dykes and flows of andesitic composition are intercalated with pyroclastic rocks. They are characterized by a gray fine-grained matrix with some phenocrysts of pyroxene and amphibole (up to 35%). They show evidence of silicification and present amygdules filled by zeolites. Textures are mainly intersertal, glomeroporphyritic (PI) and subophitic. Compositionally they vary between 20 and 41% plagioclase (An₇₀-An₅₂), 36% augite, up to 35% hornblende, 9.6% chlorite (replacing augite and hornblende) and ~10% quartz.

5.1.3 Dacitic Domes

Several cone-shaped domes are exposed in the study area and are represented by the Cerro Tusa, Cerro Bravo, Cerro Sillon and Cerro Morro Alegre hills (**Figure 2A,C, 3E**). These domes intrude the post Oligocene siliciclastic rocks of the Amagá Formation, as well as explosive and effusive rocks of the Combia volcanic complex. They are characterized by a beige matrix composed of volcanic glass and plagioclase, and subhedral hornblende and augite phenocrysts up to 3mm (altered to biotite **Figure 3F**). Textures include porphyritic, seriated, pilotaxitic and glomeroporphyritic plagioclase. Plagioclase modal abundance range between 30 and 70% (An₄₀-An₄₅) with oscillatory and undulatory zoning (the texture characteristics of deformation and disequilibrium processes); there is also between 9 and 20% hornblende, 3 and 16% quartz, 1 and 20% clinopyroxene, and 2 to 15% biotite. Zircon is present as an accessory mineral, and epidote is the characteristic alteration mineral.

5.1.4 Pyroclastic and volcanoclastic rocks

Pyroclastic rocks were studied at two main localities near the towns of Fredonia and Bolombolo (**Figure 2A**). A stratigraphic column was surveyed at the El Molino creek in Fredonia (**Figure 2D**); in the Bolombolo location the strong deformation does not allow to build a stratigraphic column, and the main lithology was described and sampled.

5.1.4.1 Fredonia region

A stratigraphic column with a total thickness of 153 m was surveyed at the El Molino Creek (**Figure 2D**) in this section; the outcrops are continuous, five main lithologies were recognized, which vary between agglomerates, lapillistones, tuffs, lahar deposits, and andesitic dykes. The bottom of the sequence is a lahar (secondary volcanoclastic) deposit with channel shapes and thicknesses between 0.5 and 1 m, while the garnet-bearing tuffs are representative of the column top. The agglomerates correspond to the thickest layers of the stratigraphic columns (up to 12 m) and are characterized by massive structure; lapillistone and tuffs comprise thinner layers (up to 50 cm) with tabular beds; andesitic dykes (<1 m) cut some pyroclastic rocks.

Secondary volcanoclastic deposits are characterized by fragments up to 2 m in diameter; these fragments are dominantly subangular and non-spheric (**Figure 3G**). They are composed of the juvenile and accidental fragments of black and green basalts and andesites; the tuffaceous matrix is characterized by its poor sorting and high porosity, and is composed of crystals of plagioclase, pyroxene, hornblende and volcanic glass. Some hornblende crystals are rusty and are being replaced by chlorite and biotite (**Figure 4H**). These rocks have generally normal gradation, becoming more fine-grained up section, but also show a chaotic internal configuration that resembles a volcanic debris flow (lahar).

The agglomerates are common through the whole section. They are characterized by rounded and sub-spherical fragments, with sizes varying between 1 and 50 cm, which is characteristic of coarse lapilli and medium blocks. The blocks are composed of juvenile black basalts, andesites, and tuffs. The matrix is made of volcanic glass, pyroxene, plagioclase, and hornblende of ash to lapilli size. At the top of the section, the agglomerates include porphyritic rocks, oxy-hornblende, and garnet. An angular discordance is observed between the agglomerates and the overlying tuff.

The tuffs are comprised of crystal and lithic fragments whose sizes vary between 0.5 and 2 cm (**Figure 3I**). The composition at the bottom of the sequence includes juvenile and accessory fragments of angular to sub-rounded basalts, andesites, tuffs, and accidental fragments related to sedimentary rocks (sandstones); some crystals of augite, hornblende, and plagioclase (An40-47) are evidenced. The tuffs at the top of the sequence are characterized by porphyritic fragments, oxy-hornblende and both pink and translucent garnets, which are euhedral crystals without corrosive boundaries (**Figure 3J**).

5.1.4.2 Bolombolo region

This location is characterized by relatively finer grained pyroclastic rocks. Agglomerates were mainly found on the eastern flank of Cauca canyon, while tuffaceous rocks are concentrated on the western side (with some columnar structures, **Figure 3K**). The agglomerates are characterized by rounded to sub-rounded juvenile and accessory fragments, that vary between 5 cm and 1 m (blocks) of black basalts mainly embedded in a medium lapilli matrix which shows flow texture; layers vary in thickness between 0.5 and 2 m. Two different types of tuffs are recognized. One of beige color, crystal-rich, matrix supported with angular to sub-rounded juvenile and accessory fragments varying in size between 0.2 and 1 cm and composed of black basaltic fragments, gray tuffs, and crystals (plagioclase, pyroxene, hornblende) with layer thicknesses between 0.1 and 2.0 m, massive layers and incinerated trees and leaves are common. The second tuffs are black in color, composed of angular (fragmented) crystals of augite and olivine as well as sub-rounded volcanic lithics, which vary in size between 0.1 and 2 cm, with layer thicknesses between 20 and 50 cm. The tuffs are fragmental, lamellar with a vitreous matrix showing flow textures. Generally, the volcanic glass has been replaced by paragonite (**Figure 3L**).

5.1.5 Sedimentary rocks

In the Fredonia area, several massive thick packages (up to 1 m) of matrix-supported rounded conglomerates are found intercalated with tuffs. They are poorly sorted with clasts up to 5 cm, mainly composed of milky quartz, black basalts, and andesites to porphyritic andesites. The matrix is sub-rounded, fine to medium size sand, and includes quartz, lithic fragments and some crystals of pyroxene (probably augite), amphibole and epidote.

In the Bolombolo section, vertical layers of conglomerates, sandstone, and mudstone are common. Conglomerates are rounded, clast-supported, with sizes up to 15 cm (pebble), and

composed primarily of chert (black and orange), black basalts, schists, and quartzites. Sandstones are coarse to medium grained size, primarily composed of lithic fragments, and some crystals (pyroxene, amphibole, and epidote). Mudstones vary between beige to violet in color (mottled) and contain some sheets of fossils and tree fragments.

5.1.6 Porphyries

Porphyritic rocks with andesitic to dacitic composition crop out along most of the Cauca depression (**Figure 1,2**). These rocks are intruding the Triassic and Cretaceous-age basement, and deformed rocks from the Amagá Formation. These bodies are characterized by crystals embedded in a gray fine-grained crystal matrix and are composed of ~58% euhedral to subeuhedral plagioclase phenocrysts (up to 5 mm), euhedral hornblende (35%), up to 3% subhedral quartz, 3% biotite, and ~3% subhedral pyroxene. Accessory minerals include zircon, apatite, and secondary chlorite is formed after hornblende and pyroxene, with accessory minerals including zircon and apatite; pyrite is also common.

5.2 Geochronology

LA-ICP-MS U-Pb zircon ages were determined for seven samples including two tuffs, one dacite dome-like sample, three porphyries and one epiclastic rock. In the Fredonia section, zircons were obtained from the lower epi-volcanoclastic rock unit and upper garnet-bearing tuff (see stratigraphic column; **Figure 2D**), and from the Cerro Bravo volcanic dome (dacite). Ages determined for the Bolombolo - La Pintada section come from one tuff collected on the western flank of the Cauca River depression, as well as the Pintada, Marmato and La Felisa porphyries (**Figure 2B**).

Magmatic zircons from the Combia volcanic complex vary between euhedral to subhedral prismatic crystals with sizes between 50 and 450 μm , and their length: width (l: w) ratios are between 2:1 and 6:1. Cathodoluminescence (CL) images display oscillatory zoning and Th/U ratios range from 0.1 to 2.8, which are typical of magmatic zircons (Vavra et al., 1999; Rubatto, 2002). Particular characteristics of zircons are described in each sample when necessary.

5.2.1 Fredonia region

Twenty-eight zircons were analyzed from an epi-volcanoclastic rock from the Fredonia area (Sample FQM-01), which is interpreted as a lahar deposit. Zircons yield a weighted average

$^{206}\text{Pb}/^{238}\text{U}$ age of 8.2 ± 0.3 Ma (2σ , $n=3$) (**Figure 4 A**), which is taken as the maximum depositional age. Some crystals are bright in CL and lack internal zoning patterns characteristic of a metamorphic origin (Vavra et al., 1999) and show ages between 250 and 2575 Ma, as well as Cretaceous ages (100-140 Ma), which may be related to the host metamorphic and igneous rocks. Ages of 11 - 12 Ma were also obtained and may be related to an older magmatic arc located west of the Combia volcanic complex; these ages are also related to high ^{204}Pb content, which was difficult to correct for.

Thirty-two zircons were analyzed from a garnet-bearing tuff (sample CQM-28B), and yielded a weighted average $^{206}\text{Pb}/^{238}\text{U}$ age of 8.2 ± 0.1 Ma ($n=20$) (**Figure 4 B**), which we consider the maximum depositional age, and due to the concordant ages, this may be related to volcanic activity.

Fifteen zircons were analyzed from a sample of an andesitic dome (Sample FCB-03) that is thought to represent former volcanic necks that supplied the volcanic materials present in the area. Some crystals show little dotted oscillatory overgrowth in the grain edges, with oscillatory nucleus. Zircons yielded a weighted average $^{206}\text{Pb}/^{238}\text{U}$ age of 7.6 ± 0.1 Ma ($n=7$), suggesting magmatic crystallization (**Figure 4 C**). The remaining analyzed crystals are characterized by bright CL and lack of zoning patterns and are considered as inherited zircons as they yielded ages between 58 and 1383 Ma, whose provenance may be related to the basement host rocks.

5.2.2 Bolombolo-La Pintada region

Twenty-nine zircons from a tuff (Sample CAB-10) were analyzed. Zircons yielded a weighted average $^{206}\text{Pb}/^{238}\text{U}$ age of 8.3 ± 0.2 Ma ($n=21$), which are interpreted as the maximum depositional age (**Figure 4 D**). Three zircons yielded ages of ~ 75 Ma, similar to the ages of the local basement.

Forty-five zircons were analyzed from a dacitic porphyry (Sample PCF-02) sampled in the La Pintada region. Zircons yielded a weighted average $^{206}\text{Pb}/^{238}\text{U}$ age of 5.2 ± 0.2 Ma ($n=8$) (**Figure 5 A**). Some crystals show oscillatory overgrowths on inherited cores, whose ages vary between 40 and 2500 Ma and are likely derived from local host rocks (supplementary data 1).

Thirty-eight zircons were analyzed from a dacitic porphyry (Sample PM-01) sampled in the

Marmato region. Zircons yield a weighted average age of 6.0 ± 0.1 Ma ($n=35$) which is taken as the magmatic crystallization age (**Figure 5 B**).

Forty zircons were analyzed from another dacitic porphyry (Sample LF-01) sampled in the La Felisa region. A weighted average age of 6.2 ± 0.1 Ma ($n=24$) was obtained and can be related to the magmatic crystallization (**Figure 5 C**). Some crystals show inherited cores with ages between 170 and 1500 Ma and may be related to the host rocks (Supplementary data 1).

5.3 Geochemistry

Samples were collected in the same Fredonia and Bolombolo - La Pintada sections. The analyzed samples do not show strong elemental mobility, as they display well correlated variation in Harker bi-variate diagrams that include Zr as the immobile element. These diagrams also show two main differentiation trends, one related to tholeiitic to calc-alkaline signatures, and the other of adakitic affinity (**Figure 6**).

5.3.1 Basaltic and andesitic flows and dykes

Seven basaltic flows, five andesitic dykes and lava flows, and one gabbro are characterized by SiO_2 values between 48.2 and 63.3 wt%, with total alkalis ($\text{Na}_2\text{O}+\text{K}_2\text{O}$) between 2.4 and 8.8 wt%; FeO_t varies between 4.5 and 11.1 wt%; CaO, and MgO vary between 5.4 and 12.2 wt% and 1.9 and 8.8 wt% respectively. Samples are classified as basalts and andesites (with one trachy-andesitic rock) (**Figure 7 A**), with tholeiitic to calc-alkaline affinity (**Figures 7 B**).

Chondrite normalized Rare Earth Element (REE) patterns can also be divided into two main groups observed in the Harker-type bivariate diagrams. The first group includes the basaltic rocks and is characterized by light REE (LREE) enrichment reflected in $(\text{La}/\text{Sm})_n$ from 1.35 to 2.9, and $(\text{La}/\text{Yb})_n$ from 2.0 to 6.4, and a relatively flat heavy REE (HREE) pattern with $(\text{Gd}/\text{Yb})_n$ ratios between 1.3 and 2.0. Subtle negative Eu anomalies (Eu/Eu^*) are observed, with values between 0.9 and 1.1 (**Figure 8 A**). The second group includes two samples, one andesite, and one trachy-andesite; these are characterized by strong enrichment in LREE with $(\text{La}/\text{Sm})_n$ ratios between 3.1 and 3.3 and $(\text{La}/\text{Yb})_n$ between 9.3 and 12.3, and depleted HREE, with $(\text{Gd}/\text{Yb})_n$ ratios between 1.96 and 2.2. Slightly positive Eu anomalies are also observed, with values between 1.1 and 1.2 (**Figure 8 A**). Multi-element diagrams,

normalized to primitive mantle, have a well-defined negative Nb and Ti anomalies, relative depletion in high field strength elements (HFSE) and enrichment in Ba and U (**Figure 8 B**). Both groups are also characterized by different Sr/Y ratios. The basaltic group has values between 19 and 50, and the andesite and trachy-andesite have higher values, varying between 95 and 102 (**Figure 9**).

The gabbroic dyke (Sample BQP-07) is classified as a basalt, and has the same major element geochemical characteristics of the basalts. This sample is characterized by low LREE enrichment, with $(La/Sm)_n$ of 1.4 and $(La/Yb)_n$ of 2.5, and relatively flat HREE flat patterns, with $(Gd/Yb)_n$ ratios of 1.5, and a small negative Eu anomaly of 0.8.

5.3.2 Dacitic Domes

The two samples from the volcanic domes are characterized by SiO_2 contents between 65.2 and 66.7 wt%, total alkalis between 6.1 and 6.5 wt%, and are then classified as dacites (**Figure 7 A**). FeO_t varies between 2.2 and 3.7 wt%, whereas CaO and MgO vary between 3.7 and 4.1wt% and 0.2 and 0.3 wt% respectively. These rocks belong to the calc-alkaline series (**Figure 7 B**).

REE patterns are characterized by LREE enrichment with $(La/Sm)_n$ between 4.6 -5.4, and $(La/Yb)_n$ between 7.6 and 9.8, with relatively flat HREE pattern and $(Gd/Yb)_n$ ratios between 1.1 and 1.2. The samples have flat to slightly positive Eu anomaly (Eu/Eu^*), characterized by values between 1.0 and 1.2 (**Figure 8 A**). Multi-element plots have well-defined negative Nb and Ti anomalies, relative depletion in HFSE, and enrichment in Ba and U (**Figure 8 C**), characteristic of a subduction related setting. The Sr/Y varies between 36 and 53 and is therefore similar to the basaltic rocks described above, with one sample having an adakite-like signature (**Figure 9**).

5.3.3 Porphyries

The three porphyritic samples are characterized by SiO_2 values between 54.6 and 66.1 wt%, with total alkalis between 5.9 and 10.4 wt%, and are therefore classified as andesites to trachy-andesites (**Figure 7 A**). FeO_t varies between 3.0 and 5.6 wt%, whereas CaO and MgO vary between 4.0 and 5.8 wt% and 1.0 and 2.2 wt% respectively. These samples follow a calc-alkaline affinity (**Figure 7 B**).

REE patterns are characterized by high LREE enrichment, with $(La/Sm)_n$ between 2.9 and

3.3, and $(La/Yb)_n$ between 6.9 and 22.98. The HREE shows depleted to flat patterns with $(Gd/Yb)_n$ ratios between 1.6 and 4.0, and an absence of an Eu anomaly (**Figure 8C**). Multi-element plots show that the samples are characterized by well-defined negative Nb and Ti anomalies, relative depletion in HFSE (one sample very depleted, identified as PCF-01), and enrichment in Ba and U (**Figure 8D**), characteristic of a subduction related setting. The Sr/Y ratio varies between low values like ~38 and high values as 151 (**Figure 9**).

5.3.4 Pyroclastic rocks

The five pyroclastic samples are characterized by SiO_2 values between 47.0 and 61.6 wt%, with total alkalis between 2.5 and 7.1 wt%, which classify them as basalts and andesites (**Figure 7A**). FeO_t varies between 5.8 and 9.5 wt%, whereas CaO and MgO vary between 4.5 and 7.9 wt% and 0.8 and 4.2 wt% respectively, so they plot within the tholeiitic and calc-alkaline series (**Figure 7B**).

REE patterns are characterized by LREE enrichment, with $(La/Sm)_n$ between 1.55 and 2.45, and $(La/Yb)_n$ between 2.38 and 4.69. They also show a relatively flat HREE pattern, with $(Gd/Yb)_n$ between 1.4 and 1.5, and lack an Eu anomaly (**Figure 8C**). Multi-element plots have well-defined negative Nb and Ti anomalies, with relative depletion in HFSE and enrichment in Ba and U (**Figure 8D**), which is characteristic of a subduction related setting. The Sr/Y ratios are characterized by low values, varying between 13 and 31 (**Figure 9**).

5.4 Hf Isotopes

Hf isotopes were determined for a selected group of samples that were also analyzed for their U-Pb ages. The pyroclastic related samples, which include garnet-bearing tuffs, tuffs, samples from lahar deposits, and a dacitic dome (Samples CQM-28B, CAB-10, FQM-01, and FCB-03) yielded a small range of crystallization ages between 7.6 and 8.3 Ma, characterized by $^{176}Hf/^{177}Hf_{(i)}$ ratios between 0.282173 and 0.283104, and initial $\epsilon Hf_{(i)}$ values between +3.3 and +11.5 (**Figure 10A**). Inherited zircons, with ages between 258 and 1000 Ma, are characterized by subchondritic $\epsilon Hf_{(i)}$ values between -5.5 and -1.5.

One andesitic porphyry (sample PCF-02) that yielded an age of 5.2 Ma is characterized by $^{176}Hf/^{177}Hf_{(i)}$ ratios between 0.282759 and 0.282969, and has a very wide range of $\epsilon Hf_{(i)}$ values between -0.9 and +6.3 (**Figure 10A**). Inherited zircons have ages between 230 and 44 Ma, and $\epsilon Hf_{(i)}$ values between -2 and +9.6.

5.5 Whole rock Sr-Nd isotopes

Whole rock Sr-Nd analysis was obtained from basalts, andesites, and porphyritic samples related to the Combia volcanic complex. One basalt and one gabbro (samples BQP-03, BQP-07), with ages ca 9 Ma (stratigraphic correlation), yield very restricted isotopic ranges, with initial $^{87}\text{Sr}/^{86}\text{Sr}$ ranging between 0.704187 and 0.704218, and initial $^{143}\text{Nd}/^{144}\text{Nd}$ values between 0.512858 and 0.512860 ($\epsilon\text{Nd}_{(t)}$ +4.53 - +4.55; **Figure 10B**). The andesite samples FCC-03 and FQM-03, with ages of ~8.2 Ma (by stratigraphic control; interlayered with tuffs), have initial $^{87}\text{Sr}/^{86}\text{Sr}$ values between 0.705019 and 0.705327, and initial $^{143}\text{Nd}/^{144}\text{Nd}$ values between 0.512610 and 0.512655 ($\epsilon\text{Nd}_{(t)}$ -0.35 - +0.52; **Figure 10B**). Andesitic porphyritic rocks (Sample CAB-11), with age ca 7 Ma (by lithologic correlation), have a $^{87}\text{Sr}/^{86}\text{Sr}$ ratio of 0.704296, and $^{143}\text{Nd}/^{144}\text{Nd}$ values of 0.512852 ($\epsilon\text{Nd}_{(t)}$ +4.34; **Figure 10B**).

6. Discussion

6.1 Petrogenesis

The different magmatic units of the Combia volcanic complex in the studied area record contrasting petrogenetic origins, and are discussed below. The basalts represent the oldest eruptive phase at ca. 9 Ma, as they are exposed at the bottom of volcanic sequences, and intrude the Oligocene-Miocene siliciclastic rocks of the Amagá Fm. Basalts include plagioclase, augite, and olivine, and have a tholeiitic composition that suggests a relatively dry mantle source. In contrast, the younger and overlying major sequence of intercalated andesites and pyroclastic rocks including tuffs, agglomerates, and breccias that crystallized by ~ 8.3 Ma (Samples CQM-28B, and CAB-10), contains hydrated minerals such as hornblende and oxyhornblende, as well as biotite, which are more likely related to water-rich magmas of calc-alkaline affinity. The porphyritic rocks also include hornblende and biotite, which are also characteristic of wet magmas.

The presence of euhedral garnet-bearing tuffs without reaction boundaries (**Figure 3J**), coexisting with hornblende and clino-pyroxene as liquid phase on the top of the sequence, indicate deep wet mantle melting and a fast magmatic rise (Harangi et al., 2001). This tuff, together with others reported by Ramirez et al. (2006), and garnet-bearing basalts and porphyries (Tejada et al., 2007), re-inforce the scenario of deep melting (ca. 40 km) and a rapid magma ascent to a shallow magmatic chamber (Bissig et al., 2017), which is also characteristic of extensional settings that facilitate magma transport across the crust

(Harangi et al., 2001). In addition to garnet, the high percentage of plagioclase with disequilibrium textures, such as oscillatory zoning, in which the plagioclase shows various growth phases, are associated to fast ascent of magma from depth to the surface (La Spina et al., 2016). Although host metamorphic rocks (e.g., Arquia and Cajamarca Complexes) are also characterized by the presence of garnet, the absence of other minerals like muscovite, epidote, graphite, and chlorite or lithic fragments in the Combia volcanic complex rocks, also confirm that they do not represent incorporated xenocrystals.

Bivariate diagrams including Zr vs. FeO, MgO, CaO, Sr, K₂O and TiO₂ (**Figure 6**) confirm the existence of at least two main magmatic series characterized by a particular differentiation trend. The first trend is consistent with tholeiitic to calc-alkaline affinity that includes basalts, andesites and explosive rocks; and the second trend is consists of andesites and porphyritic rocks, which have shown an adakite signature. From field relations it is clear that the adakite-like signature rocks intrude the tholeiitic ones, but their relations with the calc-alkaline rocks are not entirely clear.

The geochemical and isotopic signatures of the basaltic, andesitic and pyroclastic rocks from the Combia volcanic complex are characteristic of a convergent margin setting, including the Nb and Ti negative anomalies and relatively high Large Ion Lithophile Elements (LILE) concentrations. The Ti negative anomalies are lower in the basaltic units than in andesitic, pyroclastic, and porphyritic rocks, which may be related to the more limited fluid presence in the former. Such compositional patterns have also been recorded in other volcanic sequences related to the Combia volcanic complex (Bissig et al., 2017; Borrero and Toro-Toro, 2016; Leal-Mejía, 2011; Rodríguez and Zapata, 2014; Tejada et al., 2007).

In general all the analyzed samples fall into the mantle array trend in the Sr-Nd isotopic diagram, which clearly indicates a major mantle contribution. Basaltic and gabbroic rocks with tholeiitic signature have positive $\epsilon_{\text{Nd}(t)}$ and $^{87}\text{Sr}/^{86}\text{Sr}(t)$ below 0.7045, which are characteristic of mostly mantle composition mixed with more limited radiogenic sources (**Figure 10 B**). Conversely, andesitic rocks with calc-alkaline signature are characterized by $\epsilon_{\text{Nd}(t)}$ values close to zero and $^{87}\text{Sr}/^{86}\text{Sr}(t)$ values higher than 0.7045. The pyroclastic and dacitic (dome-like) rocks with calc-alkaline signature show positive $\epsilon_{\text{Hf}(t)}$, which are also typical of mantle-derived magmas with some crustal input.

These isotopic differences can be related to variations in mantle and continental crust input during magma genesis. The characteristics of the andesitic rocks are related to higher

amount of assimilation and homogenization that may be associated to deeper magma chambers (DePaolo and Wasserburg, 1976). Available isotopic constraints from other localities of the Combia volcanic complex are characterized by $\epsilon\text{Nd}_{(i)}$ values between -0.9 and 11 and $^{87}\text{Sr}/^{86}\text{Sr}_{(i)}$ below 0.7045 (Leal-Mejía, 2011; Ordoñez and Pimentel, 2001), resembling the aforementioned pattern.

Adakite-like composition was found in calc-alkaline andesites and trachyandesite samples, with ages between 5.2 Ma and 8.3 Ma. They are also characterized by Al_2O_3 and Na_2O between 16.3-20.1 and 3.2-4.5 respectively, Sr values between 635 and 1474, Y and Yb values between 7-24 and 0.39-2.65 respectively, and Sr/Y ratios between 36 and 151. The isotopic signature of a single porphyry with adakite-like signature is characterized by positive $\epsilon\text{Nd}_{(i)}$, $^{87}\text{Sr}/^{86}\text{Sr}_{(i)}$ of 0.704301, and positive $\epsilon\text{Hf}_{(i)}$ values. Other Miocene porphyritic bodies associated with the Combia volcanic complex, with ages between 8.8 and 7.2 Ma, have shown an adakite-like composition, with $\epsilon\text{Nd}_{(i)}$ values between +2.2 and +6.1 and $^{87}\text{Sr}/^{86}\text{Sr}_{(i)}$ spanning from 0.70398 to 0.704599 (Borrero and Toro-Toro, 2016; Leal-Mejía, 2011; Tassinari et al., 2008), which is also characteristic of the mantle/crust interactions.

Adakites or adakite-like compositions had been related to different mechanisms and processes, including oceanic slab melting triggered by thermally-disturbed young oceanic crust (<5Ma), subduction initiation or oceanic ridge subduction (Castillo et al., 1999; Defant and Drummond, 1990; Peacock et al., 1994). Processes within the upper plate include differentiation of mantle-derived magmas in normal (35 km thick) continental crust (Castillo, 2012; Dai et al., 2017), partial melting of mafic continental crust at high pressures (Macpherson et al., 2006), or high-pressure magmatic differentiation associated to thick crust (Bachmann et al., 2005; Chiaradia, 2009). We discard melting of oceanic crust due to the lack of high Mg# (7-30), Cr (1–32), Ni (2-7) and more juvenile isotopic signature would be achieved by slab melt during the ascent towards the mantle wedge (Defant and Drummond, 1990), which is not seen in the analyzed adakite. Additionally, the age of the oceanic crust subducting beneath the northern Andes during arc growth must be older than 5 Ma (Lonsdale, 2005), which also restricts slab melting as a feasible mechanism.

Strong differentiation is also discarded as there is no evidence of highly silicic and potassic compositions in the Combia volcanic complex. Melting of lower mafic crust associated with crustal delamination is also discarded as oblique convergence since the Eocene (Bayona et al., 2012) limits strong thickening and causes a highly heterogeneous crust (see next

subsection), and arc magmatism was strongly associated with the evolution of pull-apart systems. Another possible scenario to the adakite-like signatures, is related to the crustal erosion by subduction, which drives fore-arc material to the melting zone (Kay et al., 2005). Andesites and dacites formed by this mechanism have abnormally high Cr and Ni values (up to 200ppm), and $^{87}\text{Sr}/^{86}\text{Sr}_{(i)}$ and $^{143}\text{Nd}/^{144}\text{Nd}$ isotopic values close to MORB (Ramos et al., 2004 and references there in). Combia adakites are characterized by normal Cr and Ni values between 2.7 to 32 and 1.7 to 7.1 respectively, and $^{87}\text{Sr}/^{86}\text{Sr}_{(i)}$ and $^{143}\text{Nd}/^{144}\text{Nd}$ isotopic values of 0.704296 and 0.512852 respectively (**Figure 10 B**); also, higher $^{143}\text{Nd}/^{144}\text{Nd}$ isotopic values are found in the Western Cordillera of Colombia (Kerr et al., 2002). Additionally, we have no evidence that the magmatic arc considerably moved to the east. For these reasons we infer that subduction erosion isn't a clear scenario for the adakite-like signatures from the Combia volcanic complex.

Therefore, we favor a tectonic scenario in which mantle derived magmas were differentiated at high to moderate pressures in the garnet and amphibole stability field, explaining the moderate to high Sr/Y values in the magmatic rocks. Approximate crustal thickness values calculated for the Combia volcanic complex or its host rocks (see next subsection) are greater than 40 km, which may be compatible with an environment of deep fractionation of mantle derived magmas.

6.2 Mantle and crustal configuration

In order to evaluate variations in crustal and mantle characteristics during magma genesis and relate them with the tectonic setting, we have used the geochemical composition of the volcanic rocks as proxies for mantle temperature and crustal thickness. We chose two samples from the tholeiitic basalts composed of PI (An70-78) + CIPx \pm Ol to evaluate mantle composition and temperatures during melting. Samples BQP-10 and BQG-02 are characterized by relatively high Mg# ($100 \cdot (\text{MgO}/(\text{MgO}+\text{FeO}))$) values of 47 and 40 and FeO_t values of 9.7 and 10.4 respectively, and were considered as the less evolved samples for modelling. For the primary magmas composition, the mantle potential temperatures were estimated using the method of Lee et al. (2009), which was empirically calibrated to relatively dry mafic magmas and related the Si and Mg rock values with the temperature and pressure of magma generation. Our results suggest melting temperatures ca 1500°C. Since most of the thermometry has been calibrated for tholeiitic dry rocks, it wasn't possible to calculate the temperatures for the calc-alkaline or the more intermediate samples. However, as the

calc-alkaline rocks have higher water contents, the temperature of the andesites must be lower than the tholeiitic rocks (Grove et al., 2012; Till, 2017). Lee et al. (2009) proposed that temperatures of ca. 1200°C are characteristic of subduction-related melting at magmatic arcs in convergent margin settings, whereas higher temperatures between 1300 and 1400°C as those calculated for basaltic rocks, are rather related to mantle upwelling and melting by adiabatic decompression.

Igneous rocks formed in an arc setting in which the crustal depth is known by geophysical or xenolithic constraints have been used to calibrate empirical relationships between the Sr/Y, La/Yb, and Ce/Y whole rock ratios and Moho depth or crustal thickness (Chiaradia, 2015; Mantle and Collins, 2006; Profeta et al., 2015). Such elemental ratios reflect the stability or instability of plagioclase, amphibole and garnet as pressure increases during magmatic fractionation. When applied to the Combia volcanic complex, the oldest ca. 9 Ma basaltic rocks are characterized by relatively shallow depth of ca. 17 ± 5 km, the andesitic rocks are characterized by crustal thickness values of ca. 21 ± 4 km, the dacitic domes ca. 47 ± 4 km, and the porphyritic rocks show values higher than 51 ± 14 km (**Figure 9B**). Older Maastrichtian to Paleocene magmatic rocks in the Cauca Valley where the Combia volcanic complex is emplaced, have also yielded a crustal thickness of 55-58 km (Jaramillo et al., 2017). It's therefore suggested that crustal thickness variations are related to a heterogeneous continental crust modified by extension. Variations in crustal thickness recorded by the different magmatic rocks of the Combia volcanic complex are related to crustal thinning during local extension, so adiabatic decompression generates the older tholeiitic, hot and wet magmas of the Combia volcanic complex (**Figure 11**), while calc-alkaline rocks are formed in a typical arc environment in which input of sediments and melts from the subducted slab must have modified the mantle.

It is therefore suggested that variations in crustal thickness and mantle temperatures for the tholeiitic and calc-alkaline rocks of the Combia volcanic complex reflect an upper plate affected by local extension, that together with the existence of significant structural inheritance associated to older events, allows mantle upwelling and dry melting of deep mantle with fast emplacement of magmas at shallow depths. Simultaneously, typical convergent margin melting processes and emplacement in normal to thick crust (**Figure 11**) were also taking place in a crust that had experienced former thickening associated to the Late Cretaceous and Late Cenozoic collisional events (Jaramillo et al., 2017; León et al., 2018).

6.3 Spatio-temporal variations of Mio-Pliocene arcs and tectonic implications

The Mio-Pliocene arc magmatism in the Colombian Andes is related to the subduction of the Nazca plate. This plate was formed due to the fission of the Farallon plate at ca 23 Ma as a consequence of the divergent pull of the slab from the South American and Central American subduction zones (Lonsdale, 2005). Currently, the Nazca plate adjacent to the Colombian margin, includes oceanic crust with ages between 14 and 9 Ma, and extinct spreading ridges (Sandra and Malpelo) that have been orthogonally subducting and migrating to the northeast (ca 200 km) since the Miocene (Lonsdale, 2005; Morell, 2015). The subduction of spreading ridges is usually associated to fore-arc magmatism, metamorphism and uplift, highly heterogeneous magmatic compositions (MORB, OIB and adakite-like signatures), and the formation of a slab window associated to a magmatic hiatus above the window (Thorkelson, 1996). We still have no clear evidence of modification of the Colombian fore-arc, and seismic tomography studies in the Northwestern Andes (Chiarabba et al., 2015; Syracuse et al., 2016; Taboada et al., 2000; van der Hilst and Mann, 1994; Vargas et al., 2007) do not show a consistent low-velocity upper mantle anomaly that could be associated to the presence of a slab window. In addition, estimates of crustal and lithospheric thicknesses in the area indicate a Moho depth of around 40 km (Poveda et al., 2015) and a Lithosphere Asthenosphere Boundary of about 100 km (Blanco et al., 2017), which do not support the idea of a relatively shallow asthenospheric mantle that would be associated to a slab window. Therefore it remains to be understood how the spreading ridge systems associated to the Nazca plate behave during their subduction under the northern South American margin.

The zircon U-Pb magmatic crystallization ages presented in this contribution, together with published geochronological results obtained from the K-Ar, Ar-Ar and other zircon U-Pb ages (Bissig et al., 2017; González et al., 2010; Leal-Mejia, 2011; Lesage et al., 2013; Restrepo et al., 1981; Naranjo et al., 2018), suggest that the magmatic record of the Combia volcanic complex north of 5°N was relatively short-lived and may extend between ca. 9 Ma and 5.2 Ma. However, a small number of 11-12 Ma ages recorded in a lahar sample (sample FQM-01) may indicate the possibility of an older magmatic record, which is similar to the one immediately to the west, in the El Botón arc, which includes basalts, andesites and pyroclastic rocks mostly emplaced in the western flank of the Western Cordillera (Zapata and Rodríguez, 2011).

Rocks of the El Botón arc have shown Ar-Ar crystallization ages between 13 and 9.5 Ma, and are exposed almost 30 km to the west of the Combia volcanic complex. These rocks geochemically correspond to basalts and trachybasalts and are also characterized by relatively higher alkalis content, a smaller negative Ti, and a higher negative Ta anomaly, when compared to the Combia volcanic complex. Their geochemical characteristics and their western position probably record an arc migration, following the early initiation of arc magmatism in this region after the collision of the PCB.

Volcanic arcs in an Andean type margin are characterized by a geochemical evolution trend between tholeiitic to calc-alkaline and in some cases adakite-like signatures, over periods of tens of million years (Ducea et al., 2015), as a consequence of major changes in the subduction margin associated to both the upper and lower plates (Kay et al., 2005; Haske et al., 2006). The temporal and compositional patterns from the arc front (Combia volcanic complex) show highly heterogeneous compositions (tholeiite, calc-alkaline, adakite-like signatures) achieved in a relatively short time interval (<5Ma). We suggest that such a pattern and the variations in crustal thickness and different mantle inputs are related to strain partitioning associated to oblique subduction and to the existence of remobilized structural discontinuities that promote different mantle and crustal conditions during the magmatic evolution.

When viewed in a regional context, there seems to be major changes in the spatial distribution of Mio-Pliocene magmatic rocks north and south of 5° N. Whereas in the southern segment magmatism shows a continuous record from 24 Ma until today, in the north, the magmatic arc seems to have started later, at ca 13 Ma, and its activity ending by 5.2 Ma. Although geochemical and isotopic constraints suggest that arc magmatism in the two main arc segments are remarkably similar after 11 Ma (Bissig et al., 2017; Borrero and Toro-Toro, 2016; Gil-Rodríguez, 2014; this contribution, **Figure 8C,D**), the northern arc, as discussed here, includes tholeiitic magmatism that has not been previously observed to the south of 5°N.

The Middle Miocene to Pliocene arc magmatism of the Colombian Andes is associated to the filling of several pull-apart basins (Sierra et al., 2012; Silva-Tamayo et al., 2008). The northern pull-apart basins have shown to be wider (40 Km) when compared with the south (20 Km) (**Figure 1**). We suggest that the presence of tholeiitic rocks in the northern segments and the wider nature of pull-apart basins are linked to a more significant

extensional component. Such trend may be related to the oblique nature of the convergence, so that in the north the geometry of the margin shows a more oblique angle than in the south (**Figure 1**).

The modern magmatic arc is mostly exposed south of 5.5°N, whereas in the north, where the Combia volcanic complex is exposed, magmatic activity had already ended by 5.2 Ma. The end of the magmatism in this region is thought to be related to flattening of the subducting Nazca plate north of this latitude (Chiarabba et al., 2016; Wagner et al., 2017), Such configuration also promotes deformation in the Colombian Andes as seen in the folded nature of the Combia volcanic complex, and the exhumation and deformational record of the Western and Eastern Cordillera of Colombia (León et al., 2018; Mora et al., 2013; Parra et al., 2009).

7. Conclusions

-The new U-Pb dating, together with published Ar-Ar, and K-Ar geochronology document that magmatic activity North of 5°N was built in the Cauca Valley depression between 9 and 5.2 Ma. The existence of older zircons (11 Ma) found in volcanoclastic deposits may be related with an older Combia volcanic phase.

-The Combia volcanic complex includes three different subduction related magmatic signals: tholeiitic, calc-alkaline and adakitic. These are thought to be related to dry and wet melting conditions in a continental crust characterized by variations in its crustal thickness associated to strain partitioning; also, the geochemical evolution in a very short time interval is related to the obliqueness of the margin and the inherited faults.

-Geochemical and isotopic results suggest that magmatic rocks related to Combia volcanic complex include a significant mantle component that interacted with the older crustal material, and subsequently underwent magmatic differentiation during its evolution.

-The heterogeneous composition and short-term duration of Late Miocene magmatism in the northern Andes is a major characteristic of a convergent margin characterized by oblique convergence and strong structural inheritance.

Acknowledgments

We acknowledge the Colombian science foundation COLCIENCIAS with the grants 50491

and 51686 that supported J. S. Jaramillo through a student grant for graduate studies at the National University of Colombia and support for the field and analytical work. Additional financial support was received from the Sistema de Investigación from the National University; Project 41023.

We are grateful with the Peter Hooper GeoAnalytical Lab and the Radiogenic Isotope and Geochronology Lab (RIGL) at Washington State University in Pullman, USA, for helping us with the sample analysis. We thank Santiago Hincapié for his help during fieldwork and John J. Sanchez for his valuable comments and suggestions. Christy B. Till and Victor Ramos and the editor Andrew Kerr are acknowledged for their comments and constructive reviews of the manuscript.

Figures

Figure 1. Post Oligocene geological units of the Colombian Andes (modified from Gómez-Tapias et al., 2015) and published geochronology of magmatic rocks (U-Pb, K-Ar, Ar-Ar) (Aspden et al., 1987 and references therein; Bissig et al., 2017; Echeverri et al., 2015; Gómez-Tapias et al., 2015; González, 2010; Leal-Mejía, 2011; Lesage et al., 2013; Naranjo et al., 2018; Restrepo et al., 1981; Rodríguez and Zapata, 2012; Zapata and Rodríguez, 2011). Black arrows represent the motion vectors relative to South America Plate after Trenkamp et al. (2002). Note the north and south differences between vector's direction and magnitude. GpF: Garrapatas Fault, DPRF: Dabeiba-Pueblo Rico Fault, SPF: Silvia Pijao Fault, CAF: Cauca-Almager Fault, SJF: San Jerónimo Faul, OPF: Otú-Pericos Fault, GF: Garrapatas Fault.

Figure 2. Local geology from the studied areas. **A.** Northern segment; line between the localities of Bolombolo and Fredonia indicates the location of the profile shown in C. **B.** Southern segment. Locations of analyzed samples are indicated on the map, samples with adakite-like signature are included (Borrero and Toro-Toro, 2016; Bissig et al., 2017). **C.** Geological profile with field relations between Fredonia and Bolombolo location, showing both discordance and the intrusive relation between Combia volcanic complex rocks and Amagá Fm. **D.** Stratigraphic column from the El Molino Creek (Fredonia area); stars are the analyzed samples.

Figure 3. Field and petrographic characteristics from volcanic rocks from the Combia volcanic complex. Gl: volcanic glass; Px: Pyroxene; Pl: Plagioclase; Hb: Hornblende; Grt: Garnet. **A.** Flow basalts, **B.** Petrographic characteristic of basalts flow, **C.** Basalts with flow texture, **D.** Gabbro micro-texture, **E.** Dome shapes, **F.** Dome composition, **G.** Lahar flows, **H.** Composition of Lahar flows, **I.** Tuff deposits, **J.** Garnet-bearing tuff composition, **K.** Columnar structure in tuff, **L.** Crystal tuff composition.

Figure 4. U-Pb geochronological results from the Fredonia section and Bolombolo tuffs, including Tera-Wasserburg (left) and weighted average age diagrams (right). **A.** Lahar deposit from el Molino Creek, **B.** Garnet-bearing tuff from El Molino Creek, **C.** Dacitic dome from Cerro Bravo (Fredonia), **D.** Tuff from Bolombolo.

Figure 5. U-Pb geochronological results from the Fredonia section and Bolombolo tuffs, including Tera-Wasserburg (left) and weighted average age diagrams (right), Samples from: **A.** La Pintada Porphyry, **B.** Marmato Porphyry, **C.** La Felisa Porphyry.

Figure 6. Harker-type diagrams, where major elements are compared with Zr (immobile element). For most of the diagrams, it is possible to observe two differentiation trends (arrows).

Figure 7. Geochemical classification of the sampled rocks. **A.** Immobile element classification diagram of Winchester and Floyd, 1977 (Modified by Pearce, 1996). **B.** Zr Vs. Y classification diagram (Ross and Bédard, 2009).

Figure 8. Spider diagrams: Rare earth elements (REE) normalized to Chondrite (Nakamura, 1974) and multi-elemental diagrams normalized to Primitive Mantle (McDonough and Sun, 1995). **A.** REE diagram of basalts, andesites, and dacitic domes compared to El Botón Basalts, El Morito Basalts and Combia available data (Rodríguez and Zapata, 2014). **B.** Multi-elemental diagram of basalts, andesites and andesitic domes compared to El Botón Basalts, El Morito Basalts and Combia available data (Rodríguez and Zapata, 2014). **C.** REE diagrams of explosive and porphyritic rocks related to the Combia volcanic complex, compared to available data from porphyries (Bissig et al., 2017; Borrero and Toro-Toro, 2016; Gil-Rodríguez, 2014). **D.** Multi-elemental diagram of explosive and porphyritic rocks related to the Combia volcanic complex, compared to available data from porphyries (Bissig et al., 2017; Borrero and Toro-Toro, 2016; Gil-Rodríguez, 2014).

Figure 9. A. Sr/Y vs. Y diagram for diagnosis of an adakitic signature (Castillo et al., 1999); plots of the Combia volcanic complex volcanic and subvolcanic rocks; we used available data from Bissig et al. (2017); Borrero and Toro-Toro, (2016); Rodríguez and Zapata, (2014), B. Crustal thickness representation calculated by Mantle and Collins (2008) and Profeta et al. (2015) methods, error bars values are standard deviations associated with the average calculated from rock types .

Figure 10. Hf-Nd-Sr relations of the studied samples. **A.** ϵ_{Hf} isotopes vs age from tuffaceous, dome-like and porphyritic lithologies. **B.** Initial $^{143}\text{Nd}/^{144}\text{Nd}$ vs. $^{87}\text{Sr}/^{86}\text{Sr}$ diagram, including available data from Miocene rocks (Ordoñez and Pimentel, 2001; Tassinari et al., 2008; Leal-Mejia, 2011; Borrero and Toro-Toro, 2016; Bissig et al., 2017).

Figure 11. Schematic model of the Combia volcanic complex magmatic evolution. The strain partitioning associated with a convergent margin with high obliqueness facilitated the localized extension, and therefore the formation of pull-apart basins and the ascent of mantle-derived magmas through the crust. Both insets have the same location, first older than second.

Tables

Table 1. Geochemistry data from Combia volcanic complex rocks, Major element oxides are presented as weight per cent and trace elements as parts per million.

Sample	BCA-05	BQP-03	BQP-07	BQP-10	CQM-28B	FCC-03	FMA-01	PCF-01
Rock type	Andesite	Basalt	Gabbro	Basalt	Garnet bearing Tuff	Basalt	Porphyritic Andesite	Dacitic Phorphyry
Lat	6.023567	5.971350	5.971383	5.970167	5.898920	5.925917	5.886883	5.720850
Long	-75.847283	-75.826683	-75.823950	-75.820517	-75.689640	-75.674850	-75.697933	-75.610000
Major elements oxides (wt.%)								
SiO ₂	63.32	50.59	58.75	48.23	57.67	60.20	66.70	66.13
TiO ₂	0.37	1.28	1.42	0.65	0.69	0.72	0.22	0.41
Al ₂ O ₃	16.27	16.40	14.30	13.39	14.96	15.57	16.72	16.33
FeO*	4.48	10.98	9.69	9.69	8.45	6.98	2.24	2.97
MnO	0.07	0.17	0.17	0.16	0.17	0.13	0.09	0.05
MgO	1.92	4.12	1.76	8.75	4.02	4.09	0.16	0.98
CaO	5.35	7.94	5.46	10.85	5.73	7.00	3.67	4.32
Na ₂ O	3.25	2.96	3.50	1.72	2.22	2.29	3.16	3.71
K ₂ O	2.32	1.39	2.46	0.88	1.42	1.49	2.96	2.21
P ₂ O ₅	0.13	0.34	0.66	0.20	0.24	0.21	0.09	0.15
Sum	97.47	96.18	98.18	94.53	95.57	98.69	96.02	97.27
LOI %	1.94	3.36	1.26	4.87	3.79	0.82	3.40	1.82
Trace elements (ppm)								
Ni	4	17	2	53	8	10	4	4
V	92	300	96	262	238	143	18	40
Cr	32	26	1	253	60	145	2	5
Ga	18.6	18.8	18.5	13.5	16.7	16.6	16.2	21.1
Cu	10	150	223	148	12	17	5	4
Zn	119	109	122	73	133	108	56	99
La	12.62	7.75	14.76	4.22	10.97	12.01	19.45	13.50
Ce	20.41	16.59	31.41	8.91	19.97	19.88	28.88	23.36
Pr	2.90	2.50	4.82	1.33	2.88	3.09	3.62	3.10
Nd	11.27	11.87	22.16	6.33	12.13	12.92	12.60	12.23
Sm	2.38	3.48	6.36	1.81	2.99	3.16	2.23	2.55
Eu	0.84	1.17	1.79	0.69	0.94	1.01	0.78	0.78
Gd	1.90	4.06	7.34	2.19	3.10	3.47	1.96	1.95
Tb	0.27	0.70	1.26	0.37	0.51	0.59	0.31	0.25
Dy	1.54	4.41	7.97	2.44	3.18	3.74	1.87	1.23
Ho	0.30	0.93	1.66	0.51	0.66	0.77	0.40	0.20
Er	0.78	2.57	4.50	1.39	1.81	2.10	1.21	0.48
Tm	0.11	0.36	0.63	0.20	0.27	0.30	0.19	0.07
Yb	0.68	2.23	4.03	1.23	1.68	1.93	1.33	0.39
Lu	0.11	0.34	0.62	0.20	0.26	0.30	0.24	0.06
Ba	2659	869	1393	531	1392	1929	2775	2387
Th	2.53	1.50	2.74	0.80	2.14	2.85	4.02	3.33
Nb	5.99	3.77	7.12	1.42	4.03	4.31	7.19	4.72
Y	7.8	23.1	41.7	12.7	16.9	19.9	11.9	5.6
Hf	2.65	2.10	3.89	1.04	2.18	2.32	2.95	3.18

Ta	0.44	0.26	0.48	0.12	0.30	0.33	0.57	0.30
U	1.56	0.73	1.41	0.37	3.98	1.09	1.97	1.74
Pb	9.78	5.74	8.84	2.43	6.46	6.12	12.47	11.07
Rb	64.25	31.63	59.24	17.45	34.43	38.00	81.48	55.66
Cs	1.33	0.74	1.02	0.36	0.95	1.21	1.66	2.39
Sr	791	409	367	363	519	419	635	843
Sc	12.2	34.5	31.2	39.7	23.4	26.9	1.6	4.7
Zr	92	71	132	34	80	85	112	115
Sr/Y	101.6	17.7	8.8	28.6	30.8	21.0	53.2	151.0

Table 2. Sr-Nd Isotopes from Combia volcanic complex rocks.

Sam ple	Rock Type	Lat	Long	A ge	Rb	Sr	$^{87}\text{Sr}/$ ^{86}Sr	Err or	Sm	Nd	$^{143}\text{Nd}/$ ^{144}Nd	Err or	$^{147}\text{Sm}/$ ^{144}Nd	EN d
BQP -03	Basalt	5.97 135	- 75.82 668	9*	31. 63	408. 80	0.704 190	5	3.4 24	12.2 28	0.51286 0	8	0.16934 7	4.5 5
BQP -07	Gabbr o	5.97 138	- 75.82 395	9*	59. 24	366. 72	0.704 219	4	5.9 37	21.6 49	0.51285 8	10	0.16588 0	4.5 3
CAB -11	Andesi tic Porphy ry	6.02 332	- 75.76 195	7*	59. 46	796. 19	0.704 296	4	3.1 16	15.0 25	0.51285 2	8	0.12542 0	4.3 4
FCC -03	Andesi te	5.92 592	- 75.67 485	6*	38. 00	418. 78	0.705 332	4	3.0 07	12.6 84	0.51261 2	8	0.14336 9	- 0.3 6
FQM -03	Andesi te	5.89 538	- 75.69 315	6*	40. 05	480. 67	0.705 023	4	2.8 12	12.2 56	0.51265 7	8	0.13879 1	0.5 1

Supplementary material

Supplementary material 1. Geochronology data from Combia volcanic complex rocks

Supplementary material 2. Hf isotope data from Combia volcanic complex rocks.

References

Aspden, J. A., Mccourt, W.J. and Brook, M., 1987. Geometrical control of subduction-related magmatism: The Mesozoic and Cenozoic plutonic history of Western Colombia. *J. Geol. Soc.*, 144, 893–905.

Bachmann, O., Dungan, M.A., Bussy, F., 2005. Insights into shallow magmatic processes in large silicic magma bodies: The trace element record in the fish canyon magma body, Colorado. *Contributions to Mineralogy and Petrology*, 149, 338–349.

Bayona, G., Cardona, A., Jaramillo, C., Mora, A., Montes, C., Valencia, V., Ayala, C., Montenegro, O., Ibañez-Mejía, M., 2012. Early Paleogene magmatism in the northern

Andes: insights on the effects of oceanic plateau-continent convergence. *Earth Planet. Sci. Lett.* 331-332, 97-111.

Bissig, T., Leal-Mejía, H., Stevens, R. B., and Hart, C. J. 2017. High Sr/Y Magma Petrogenesis and the Link to Porphyry Mineralization as Revealed by Garnet-Bearing I-Type Granodiorite Porphyries of the Middle Cauca Au-Cu Belt, Colombia. *Economic Geology*, 1123, 551-568.

Black, L.P., Kamo, S.L., Allen, C.M., Aleinikoff, J.N., Davis, D.W., Korsch, R.J., Foudoulis, C., 2003. TEMORA 1: A new zircon standard for Phanerozoic U–Pb geochronology. *Chemical Geology*, 200, 155-170.

Blanco, J.F., Vargas, C.A., and Monsalve, G., 2017. Lithospheric thickness estimation beneath Northwestern South America from an S-wave receiver function analysis. *Geochemistry, Geophysics, Geosystems*, 18, 1376-1387.

Borrero, C., and Toro-Toro, L.M., 2016. Vulcanismo de afinidad adakítica en el miembro inferior de la Formación Combia Mioceno tardío al sur de la subcuenca de Amagá, noroccidente de Colombia. *Boletín de Geología*, 381, 87-100.

Bouvier, A., Vervoort, J.D., Patchett, P.J., 2008. The Lu-Hf and Sm-Nd isotopic composition of CHUR: Constraints from unequilibrated chondrites and implications for the bulk composition of terrestrial planets. *Earth and Planetary Science Letters*, 273, 48–57.

Calvache, M.L., and Williams, S., 1997. Geochemistry and petrology of the Galeras Volcanic Complex, Colombia. *Journal of Volcanology and Geothermal Research*, 77, 21-38.

Castillo, P. R., Janney, P. E., and Solidum, R. U., 1999. Petrology and geochemistry of Camiguin Island, southern Philippines: Insights to the source of adakites and other lavas in a complex arc setting. *Contributions to Mineralogy and Petrology*, 134 (1), 33-51.

Castillo, P.R., 2012. Adakite petrogenesis. *Lithos*, 134-135, 304–316.

Chang, Z., Vervoort, J.D., McClelland, W.C., Knaack, C., 2006. U-Pb dating of zircon by LA-ICP-MS. *Geochem. Geophys. Geosystems*, 7 (5), 1-14.

Chiarabba, C., De Gori, P., Faccenna, C., Speranza, F., Seccia, D., Dionicio, V., and

Prieto, G. A., 2015. Subduction system and flat slab beneath the Eastern Cordillera of Colombia. *Geochemistry, Geophysics, Geosystems*, 171, 16-27.

Chiaradia, M. 2015. Crustal thickness control on Sr/Y signatures of recent arc magmas: An Earth scale perspective. *Scientific Report*, 5, 8115; DOI: 10.1038/srep08115.

Chiaradia, M., Müntener, O., Beate, B., and Fontignie, D., 2009. Adakite-like volcanism of Ecuador: Lower crust magmatic evolution and recycling. *Contributions to Mineralogy and Petrology*, 158(5), 563-588.

Dai, H. K., Zheng, J., Zhou, X., and Griffin, W. L., 2017. Generation of continental adakitic rocks: Crystallization modeling with variable bulk partition coefficients. *Lithos*, 272, 222-231.

Defant, M.J., Drummond, M.S., 1990. Derivation of some modern arc magmas by melting of young subducted lithosphere. *Nature* 347, 662–665.

DePaolo, D. J., and Wasserburg, G. J., 1976. Nd isotopic variations and petrogenetic models. *Geophysical Research Letters*, 3 (5), 249-252.

Ducea, M.N., Saleeby, J.B., and Bergantz, G., 2015. The architecture, chemistry, and evolution of continental magmatic arcs: *Annual Review of Earth and Planetary Sciences*, 43, 299–331, doi:10.1146/annurev-earth-060614-105049.

Duque-Caro, H., 1990. The Choco Block in the northwestern corner of South America: Structural, tectonostratigraphic, and paleogeographic implications. *Journal of South American Earth Sciences*, 3 (1), 71-84.

Echeverri, S., Cardona, A., Pardo, A., Monsalve, G., Valencia, V. A., Borrero, C., ... and López, S., 2015. Regional provenance from southwestern Colombia fore-arc and intra-arc basins: Implications for Middle to Late Miocene orogeny in the Northern Andes. *Terra Nova*, 275, 356-363.

Fisher, C.M., Hanchar, J.M., Samson, S.D., Dhuime, B., Blichert-Toft, J., Vervoort, J.D., and Lam, R., 2011. Synthetic zircon doped with hafnium and rare earth elements: A reference material for in situ hafnium isotope analysis. *Chemical Geology*, 286, 32-47.

Fisher, C.M., Vervoort, J.D., and DuFrane, S.A., 2014. Accurate Hf isotope determinations

of complex zircons using the “laser ablation split stream” method. *Geochemistry, Geophysics, Geosystems (G3)*, 15, 121-139.

Fisher, R. V., and Schmincke, H.U., 1984. *Pyroclastic Rocks*. Springer-Verlag. 484p.

Gaschnig, R.M., Vervoort, J.D., Lewis, R.S., and Tikoff, B., 2011. Isotopic evolution of the Idaho batholith and Challis Intrusive Province, Northern US Cordillera. *Journal of Petrology*, 52 (12), 2397–2429.

Gil-Rodríguez, J., 2014, Petrology of the Betulia Igneous Complex, Cauca, Colombia. *Journal of South American Earth Sciences*, 56, 339-356

Gómez-Tapias, J., Nivia, Á., Montes, N.E., Almanza, M.F., Alcárcel, F.A. and Madrid, C.A. 2015. Mapa Geológico de Colombia. In: Gómez, J. and Almanza, M.F. (Editores), *Compilando la geología de Colombia: Una visión a 2015*. Servicio Geológico Colombiano, *Publicaciones Geológicas Especiales*, 33, 9–33. Bogotá.

González, H., 2010. Geoquímica, geocronología de las unidades litológicas asociadas al Sistema de Fallas Cauca–Romeral, sector centro–sur, Tomo I. INGEOMINAS, informe interno, 412 p. Medellín.

Grosse, E., 1926. Estudio Geológico del Terciario Carbonífero de Antioquia en la parte Occidental de la Cordillera Central de Colombia entre El Río Arma y Sacaojal. Dietrich Rimer, 361p. Berlin.

Grove, T. L., Till, C. B., and Krawczynski, M. J., 2012. The role of H₂O in subduction zone magmatism. *Annual Review of Earth and Planetary Sciences*, 40, 413-439.

Haschke, M., Günther, A., Melnick, D., Echtler, H., Reutter, K. J., Scheuber, E., and Oncken, O., 2006. Central and southern Andean tectonic evolution inferred from arc magmatism. In: Oncken, O., Chong, G., Franz, G., Giese, P., Götze, H.-J., Ramos, V.A., Strecker, M.R., Wigger, P. (Eds.) *The Andes*. Springer, Berlin, Heidelberg. 337-353.

Harangi, S. Z., Downes, H., Kósa, L., Szabó, C. S., Thirlwall, M. F., Mason, P. R. D., and Matthey, D., 2001. Almandine garnet in calc-alkaline volcanic rocks of the Northern Pannonian Basin (Eastern–Central Europe): Geochemistry, petrogenesis and geodynamic implications. *Journal of Petrology*, 42 (10), 1813-1843.

Herzberg, C., and Asimow, P. D., 2015. PRIMELT3 MEGA. XLSM software for primary magma calculation: Peridotite primary magma MgO contents from the liquidus to the solidus. *Geochemistry, Geophysics, Geosystems*, 16 (2), 563-578.

Janoušek, V., Farrow, C. M., and Erban, V., 2006. Interpretation of whole-rock geochemical data in igneous geochemistry: Introducing Geochemical Data Toolkit (GCDkit). *Journal of Petrology*, 47 (6), 1255-1259.

Jaramillo, J. S., Cardona, A., León, S., Valencia, V., and Vinasco, C., 2017a. Geochemistry and geochronology from Cretaceous magmatic and sedimentary rocks at 6° 35' N, western flank of the Central cordillera (Colombian Andes): Magmatic record of arc growth and collision. *Journal of South American Earth Sciences*, 76, 460-481.

Johnson, D.M., Hooper, P.R., Conrey, R.M., 1999. XRF Analysis of Rocks and Minerals for Major and Trace Elements on a Single Low Dilution Li-Tetraborate Fused Bead. *JCPDS-International Centre for Diffraction Data*, pp. 843–867.

Kay, S.M., Godoy, E., and Kurtz, A., 2005. Episodic arc migration, crustal thickening, subduction erosion, and magmatism in the south-central Andes. *Geological Society of America Bulletin*, 117, 67-88.

La Spina, G., Burton, M., Vitturi, M. D. M., and Arzilli, F., 2016. Role of syn-eruptive plagioclase disequilibrium crystallization in basaltic magma ascent dynamics. *Nature communications*, 7, 13402.

Leal-Mejía, H., 2011. Phanerozoic gold metallogeny in the Colombian Andes: A tectono-magmatic approach. Ph.D. thesis Departament de Cristal·lografia, Mineralogia i Dipòsits Minerals, Facultat de Geologia, Universitat de Barcelona, España, 1000 p.

Lee, C. T. A., Luffi, P., Plank, T., Dalton, H., and Leeman, W. P., 2009. Constraints on the depths and temperatures of basaltic magma generation on Earth and other terrestrial planets using new thermobarometers for mafic magmas. *Earth and Planetary Science Letters*, 279 (1-2), 20-33.

León, S., Cardona, A., Parra, M., Sobel, E. R., Jaramillo, J. S., Glodny, J., ... and Pardo-Trujillo, A. 2018. Transition from collisional to subduction-related regimes: An example from Neogene Panama-Nazca-South America interactions. *Tectonics*, 37 (1), 119-139.

<https://doi.org/10.1002/2017TC004785>

Lesage, G., Richards, J. P., Muehlenbachs, K., and Spell, T. L. 2013. Geochronology, geochemistry, and fluid characterization of the late Miocene Buriticá gold deposit, Antioquia Department, Colombia. *Economic Geology*, 1085, 1067-1097.

Lonsdale, P., 2005. Creation of the Cocos and Nazca plates by fission of the Farallon plate. *Tectonophysics*, 4043-4, 237-264.

Ludwig, K.R., 2012. Isoplot 3.75. A Geochronological Toolkit for Microsoft Excel. Berkeley Geochronology Center, 70p. Special Publication 4.

MacDonald, W.D., Estrada, J.J., Sierra, G.M., and González, H., 1996. Late Cenozoic tectonics and paleomagnetism of North Cauca Basin intrusions, Colombian Andes: Dual rotation modes. *Tectonophysics*, 261, 277-289.

Macpherson, C.G., Dreher, S.T., and Thirlwall, M.F., 2006. Adakites without slab melting: High pressure differentiation of island arc magma, Mindanao, the Philippines. *Earth and Planetary Science Letters* 243 (3-4), 581-593.

Mantle, G.W., Collins, W.J., 2008. Quantifying crustal thickness variations in evolving orogens: correlation between arc basalt composition and Moho depth. *Geology* 36 (1), 87- 90.

McDonough, W. F., and Sun, S. S., 1995. The composition of the Earth. *Chemical geology*, 120 (3-4), 223-253.

Montes, C., Cardona, A., Jaramillo, C., Pardo, A., Silva, J. C., Valencia, V., Ayala, C., Pérez-Angel, L. C., Rodríguez-Parra, L. A., Ramirez, V. and Niño, H., 2015. Middle Miocene closure of the Central American Seaway, *Science*, 348, 226-229.

Mora, A., Reyes-Harker, A., Rodríguez, G., Tesón, E., Ramirez-Arias, J. C., Parra, M., ... and Ibañez, M., 2013. Inversion tectonics under increasing rates of shortening and sedimentation: Cenozoic example from the Eastern Cordillera of Colombia. *Geological Society, London, Special Publications*, 377, 411-442.

Mora-Paez, H., Kellogg, J.N., Freymueller, J.T., Mencin, D., Fernandes, R.M.S., Diederix, H., LaFemina, P., Cardona-Peidrathita, L., Lizarazo, S., Peláez-Gaviria, J.R., Díaz-Mila,

F., Bohórquez-Orozco, O., Giraldo-Londoño, L., and Corchuelo-Cuervo, Y., 2019. Crustal deformation in the northern Andes – A new GPS velocity field, *Journal of South American Earth Sciences*, 89, 76-91.

Morell, K.D., 2015 Late Miocene to recent plate tectonic history of the southern Central America convergent margin. *Geochemistry, Geophysics, Geosystems*. 16, 3362-3382.

Nakamura, N., 1974. Determination of REE, Ba, Fe, Mg, Na, and K in carbonaceous and ordinary chondrites. *Geochim. Cosmochim. Acta* 38, 757-775.

Naranjo, A., Horner, J., Jahoda, R., Diamond, L. W., Castro, A., Uribe, A., ... and Weil, J., 2018. La Colosa Au Porphyry Deposit, Colombia: Mineralization Styles, Structural Controls, and Age Constraints. *Economic Geology*, 113 (3), 553-578.

Ojeda, A., and Havskov, J., 2001. Crustal structure and local seismicity in Colombia. *Journal of seismology*, 5 (4), 575-593.

Ordoñez, O. and Martins, M. 2001. Geoquímica isotópica del magmatismo reciente <11 Ma, en los andes colombianos. VII Congreso Colombiano de Geología. *Geoquímica Manizales, Colombia*, 1 - 4.

Parra, M., Mora, A., Sobel, E. R., Strecker, M. R., and González, R., 2009. Episodic orogenic front migration in the northern Andes: Constraints from low-temperature thermochronology in the Eastern Cordillera, Colombia. *Tectonics*, 28, TC4004.

Peacock, S.M., Rushmer, T., and Thompson, A.B., 1994. Partial melting of subducting oceanic crust. *Earth and Planetary Science Letters* 121 (1–2), 227–244.

Pearce, J.A., 1996. A user's guide to basalt discrimination diagrams. In: Wyman, D.A. (Ed.), *Trace Element Geochemistry of Volcanic Rocks: Applications for Massive Sulphide Exploration*. Geological Association of Canada, Short Course Notes, 12, 79-113.

Poveda, E., Monsalve, G., and Vargas, C.A., 2015. Receiver functions and crustal structure of the northwestern Andean region, Colombia. *Journal of Geophysical Research: Solid Earth*, 120, 2480-2425.

Profeta, L., Ducea, M.N., Chapman, J.B., Paterson, S.R., Henriquez-Gonzales, S.M., Kirsch, M., Petrescu, L., and DeCelles, P.G., 2015. Quantifying crustal thickness over time

in magmatic arcs. *Sci. Rep.* 5, 17786.

Ramírez, D. A., López, A., Sierra, G. M., and Toro, G. E., 2006. Edad y procedencia de las rocas volcánico sedimentarias de la Formación Combia en el Suroeste Antioqueño-Colombia. *Boletín de Ciencias de la Tierra*, 19, 9-26.

Ramos, V. A., Kay, S.M., and Singer, B.S., 2004. Las adakitas de la Cordillera Patagónica: Nuevas evidencias geoquímicas y geocronológicas. *Revista de la Asociación geológica Argentina*, 59(4), 693-706.

Restrepo, J.J.; Toussaint, J.F. y González, H., 1981. Edades MioPliocenas del magmatismo asociado a la Formación Combia. Departamentos de Antioquia y Caldas, Colombia. *Geología Norandina*, 3, 21-26.

Rodríguez, G., and Zapata, G., 2012. Características del plutonismo Mioceno superior en el segmento norte de la Cordillera Occidental e implicaciones tectónicas en el modelo geológico del noroccidente colombiano. *Boletín de Ciencias de la Tierra*, 31, 5-22.

Rodríguez, G., and Zapata, G., 2014. Descripción de una nueva unidad de lavas denominada Andesitas basálticas de El Morito-correlación regional con eventos magmáticos de arco. *Boletín de Geología*, 36(1), 85-102.

Ross, P.S., Bédard, J.H., 2009. Magmatic affinity of modern and ancient subalkaline volcanic rocks determined from trace-element discriminant diagrams. *Can. J. Earth Sci.* 46, 823-839.

Rubatto, D., 2002. Zircon trace element geochemistry: Partitioning with garnet and the link between U–Pb ages and metamorphism. *Chemical geology*, 184 (1-2), 123-138.

Sierra, G., Marín-Cerón, M. I., and MacDonald, W., 2012. Tectonic evolution of the Irra pull-apart basin evidences of slip reversals on the Romeral fault zone, northern part of Andean central cordillera, Colombia. *Boletín de Ciencias de la Tierra*, 32, 143-159.

Silva-Tamayo, J. C., Sierra, G. M., y Correa, L. G., 2008. Tectonic and climate driven fluctuations in the stratigraphic base level of a Cenozoic continental coal basin, northwestern Andes. *Journal of South American Earth Sciences*, 26 (4), 369-382.

Sláma, J., Kolesár, J., Condon, D.J., Crowley, J.L., Gerdes, A., Hanchar, J.M., Horstwood,

M.S.A., Morris, G.A., Nasdala, L., Norberg, N., Schaltegger, U., Schoene, B., Tubrett, M.N., Whitehouse, M.J., 2008. Ple sovice zircon e a new natural reference material for U-Pb and Hf isotopic microanalysis. *Chem. Geol.* 249, 1-35.

Somoza, R., 1998. Updated Nazca Farallon—South America relative motions during the last 40 My: Implications for mountain building in the central Andean region. *Journal of South American Earth Sciences*, 113, 211-215.

Syracuse, E. M., Maceira, M., Prieto, G. A., Zhang, H., and Ammon, C. J., 2016. Multiple plates subducting beneath Colombia, as illuminated by seismicity and velocity from the joint inversion of seismic and gravity data. *Earth and Planetary Science Letters*, 444, 139-149.

Taboada, A., Rivera, L.A., Fuenzalida, A., Cisternas, A., Philip, H., Bijwaard, H., Olaya, J., and Rivera, C., 2000. Geodynamics of the northern Andes: Subductions and intracontinental deformation (Colombia), *Tectonics*, 19, 787–813.

Tassinari, C.C.G., Díaz, F., and Buenaventura, J., 2008. Age and sources of gold mineralization in the Marmato mining district, NW Colombia: a Miocene-Pliocene epizonal gold deposit. *Ore Geology Reviews*, 33, 505–518.

Tejada, M., Betancourt, J., Nivia, A., Weber, M., and Gómez, J., 2007. Cartografía geológica y caracterización geoquímica de la Formación Combia en los alrededores de Jericó y Pueblorrico, departamento de Antioquia – Colombia. *Memorias XI Congreso Colombiano de Geología*. Bucaramanga.

Thorkelson, D.J., 1996. Subduction of diverging plates and the principles of slab window formation. *Tectonophysics*, 255, 47-63.

Till, C.B., 2017. A review and update of mantle thermobarometry for primitive arc magmas. *American Mineralogist*, 102, 931-947.

Toro-Toro, L.M., Alvarán-Echeverri, M., and Borrero-Peña, C.A., 2008. Rocas con afinidad adakítica al sureste de Manizales: Rasgos petrogenéticos y geoquímicos. *Boletín de Geología*, 302, 49-60.

Toussaint, J. F., 1996. *Evolución Geológica de Colombia, Cretácico*. Universidad

Nacional de Colombia. Medellín, 142.

Trenkamp, R., Kellogg, J. N., Freymueller, J. T., and Mora, H. P., 2002. Wide plate margin deformation, southern Central America and northwestern South America, CASA GPS observations. *Journal of South American Earth Sciences*, 15(2), 157-171.

van der Hilst, R. D., and Mann, P., 1994. Tectonic implications of tomographic images of subducted lithosphere beneath northwestern South America, *Geology*, 22, 451–454.

Vargas, C.A., and Mann, P., 2013. Tearing and breaking off of subducted slabs as the result of collision of the Panama Arc-Indenter with Northwestern South America. *Bulletin Seismological Society Am.*, 103 (3), 2025–2046.

Vargas, C. A., Pujades, L. G., and Montes, L., 2007. Seismic structure of South-Central Andes of Colombia by tomographic inversion. *Geofísica internacional*, 46(2), 117-127.

Vavra, G., Schmid, R., and Gebauer, D., 1999. Internal morphology, habit and U-Th-Pb microanalysis of amphibolite-to-granulite facies zircons: Geochronology of the Ivrea Zone (Southern Alps). *Contrib. Mineral. Petrol.*, 134, 380-404.

Vervoort, J.D., and Blichert-Toft, J., 1999. Evolution of the depleted mantle: Hf isotope evidence from juvenile rocks through time. *Geochimica et Cosmochimica Acta*, 63, 533–556.

Vervoort, J.D., and Patchett, P.J., 1996. Behavior of hafnium and neodymium isotopes in the crust: Constraints from Precambrian crustally derived granites. *Geochimica et Cosmochimica Acta*, 60, 3717–3733.

Vervoort, J.D., Kemp, A.I.S., Fisher, C., and Bauer, A., 2015. The rock record has it about right—no significant continental crust formation prior to 3.8 Ga. American Geophysical Union, Fall Meeting, San Francisco, Abstracts.

Wagner, L. S., Jaramillo, J. S., Ramírez-Hoyos, L. F., Monsalve, G., Cardona, A., and Becker, T. W., 2017. Transient slab flattening beneath Colombia. *Geophysical Research Letters*, 44, 6616–6623. <https://doi.org/10.1002/2017GL073981>

Williams, I.S., 1998. U-Th-Pb geochronology by Ion microprobe. In McKibben, M. A., Shanks III, W. C., and Ridley, W. I. (eds.): Applications of microanalytical techniques to

understanding mineralizing processes. *Reviews in Economic Geology*, 7, 1-35

Winchester, J.A., and Floyd, P.A., 1977. Geochemical discrimination of different magma series and their differentiation products using immobile elements. *Chem. Geol.* 20, 325-343.

Zapata, G., and Rodríguez, G., 2011. Basalto de El Botón, Miocene volcanic arc of Shoshonitic affinity to the North of Cordillera Occidental of Colombia. *Boletín de Ciencias de la Tierra* 30, 77-92.

ACCEPTED MANUSCRIPT

HIGHLIGHTS

- Short duration arc magmatism.
- Compositionally and petrogenetically heterogeneous magmatism.
- Oblique convergence magmatic tracer.
- Changing nature of the Nazca plate subduction in the Northern Andes.

ACCEPTED MANUSCRIPT

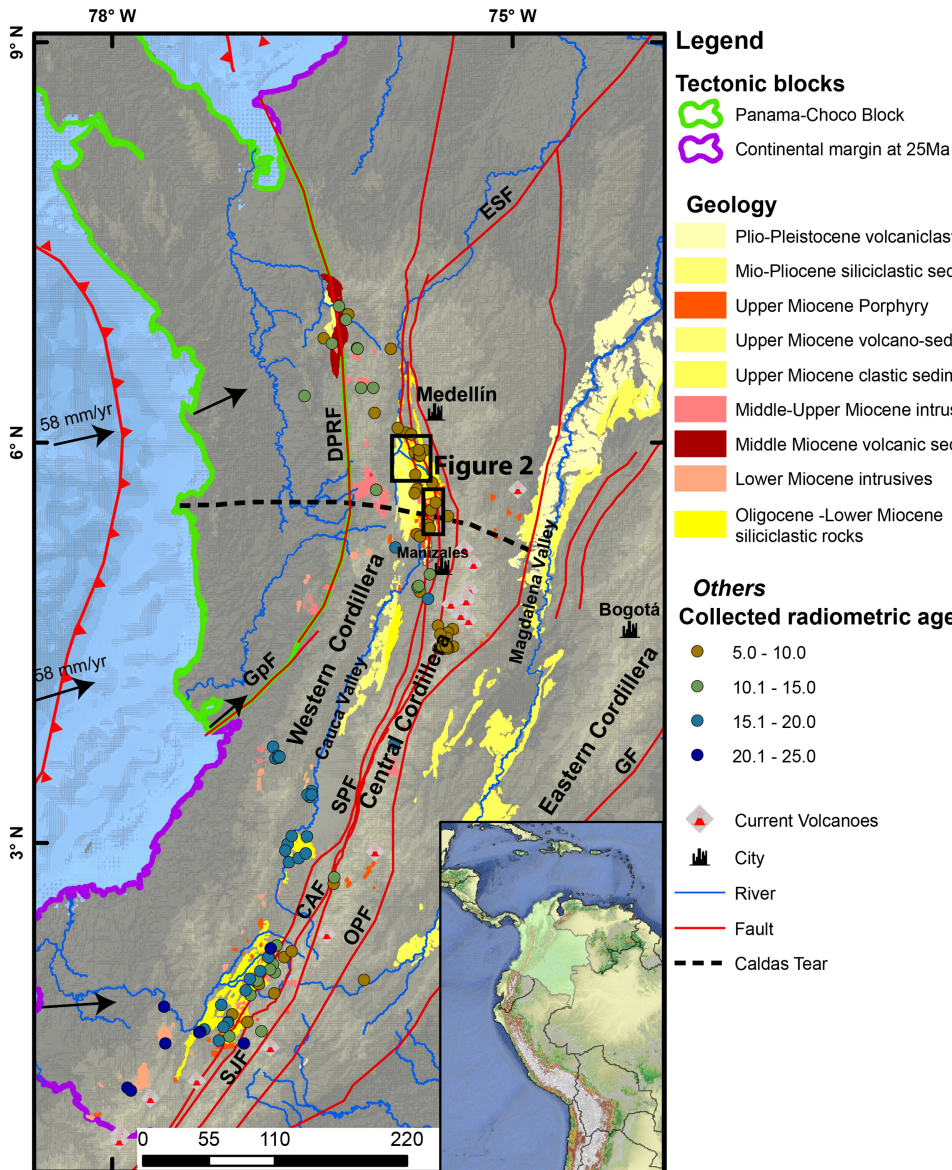


Figure 1

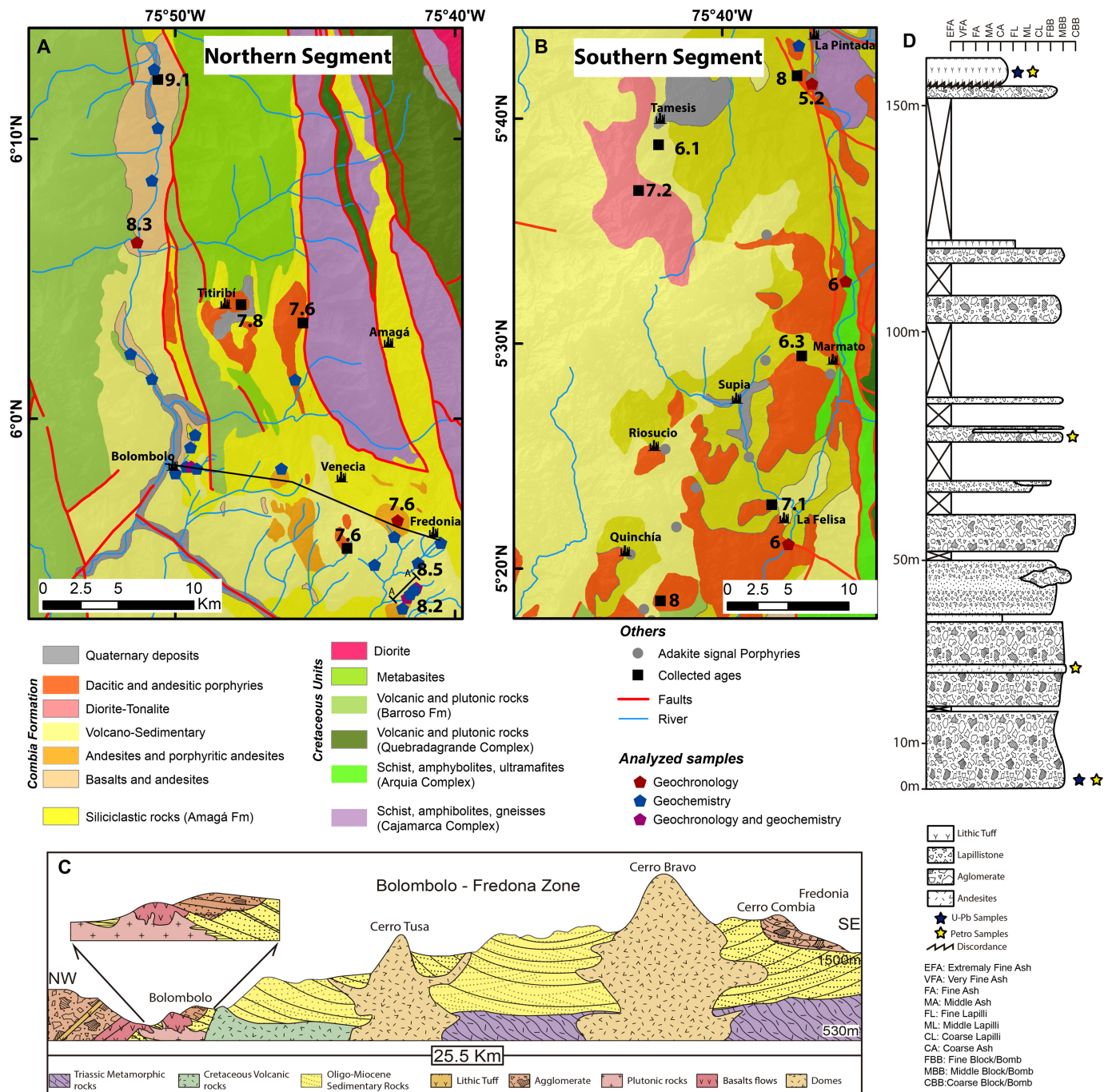


Figure 2

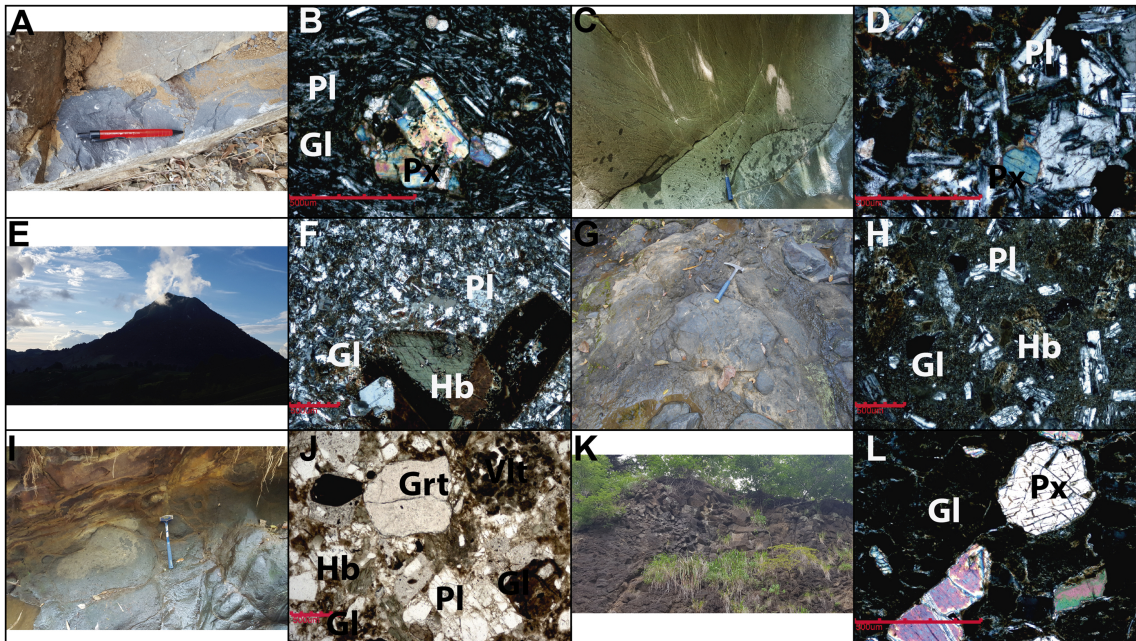


Figure 3

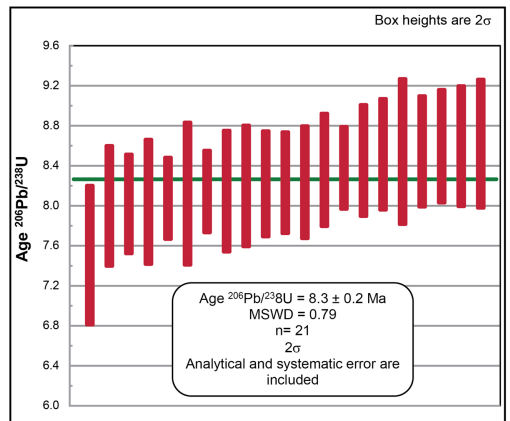
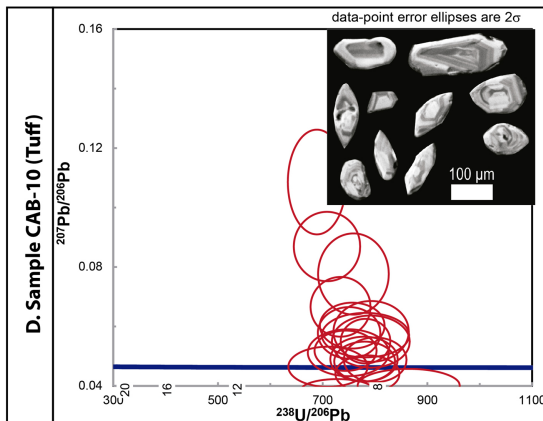
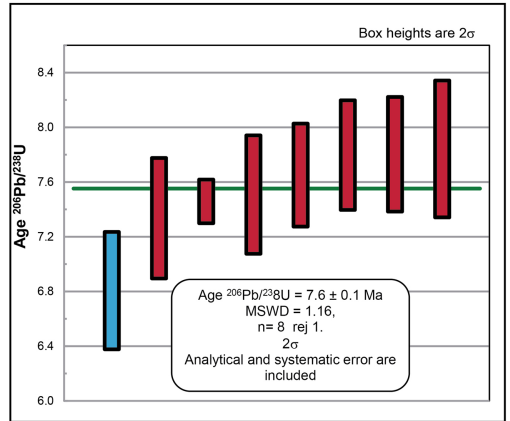
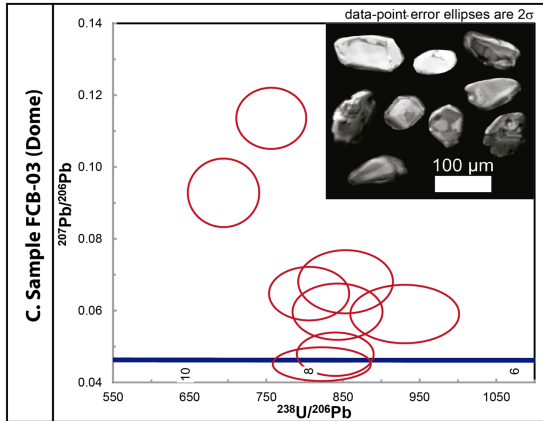
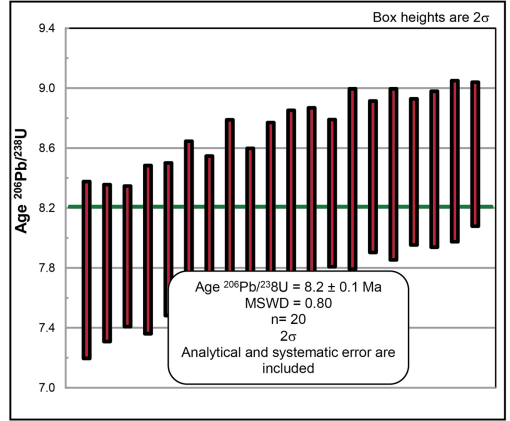
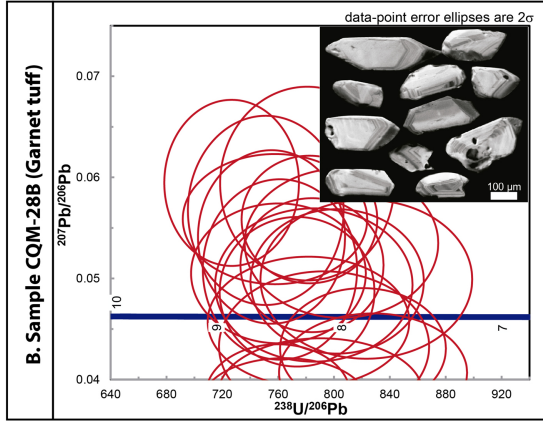
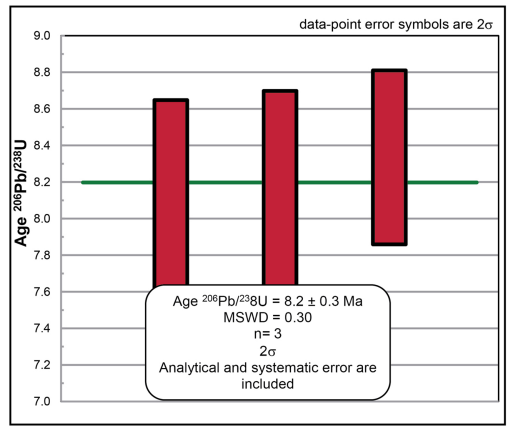
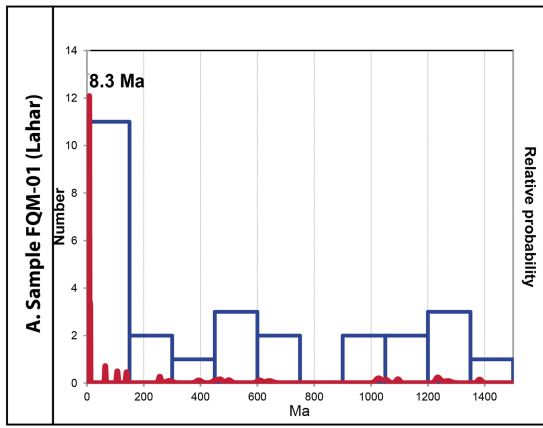


Figure 4

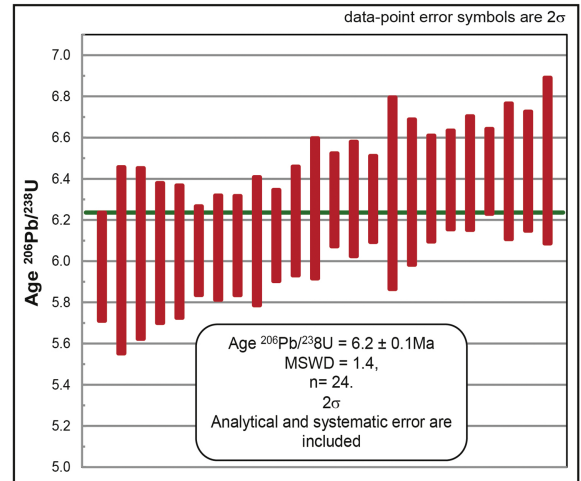
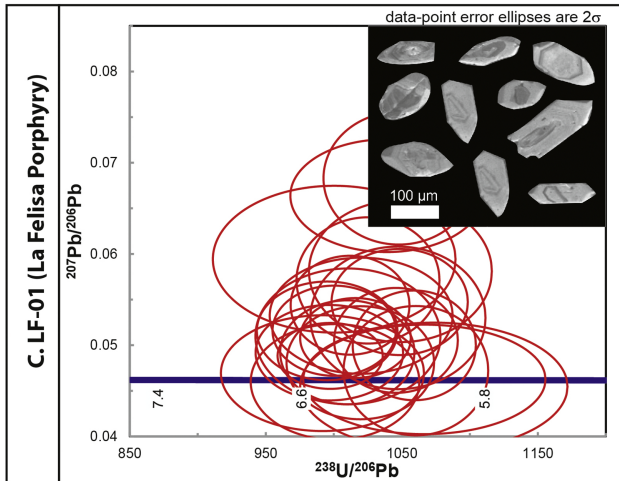
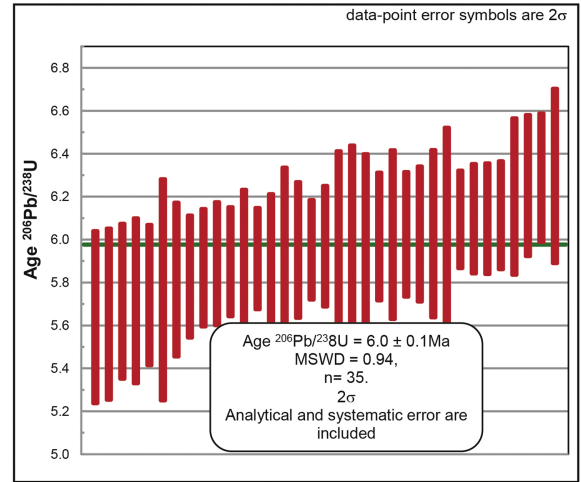
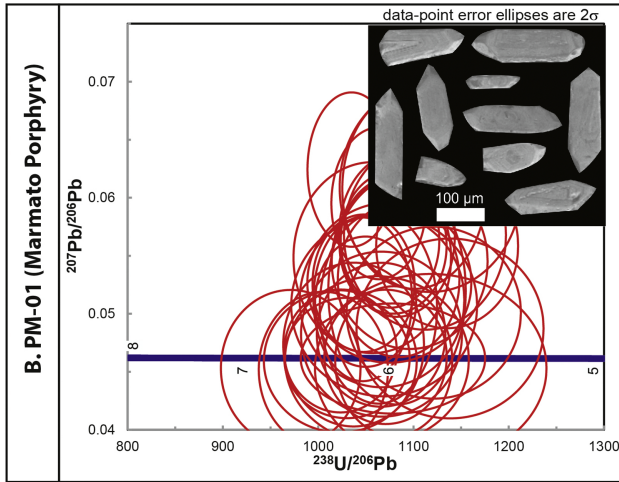
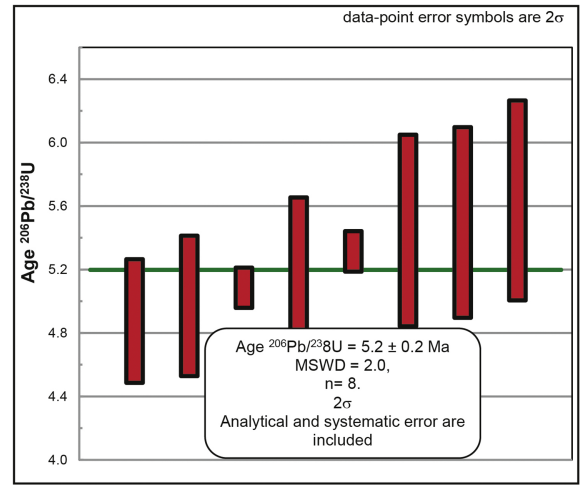
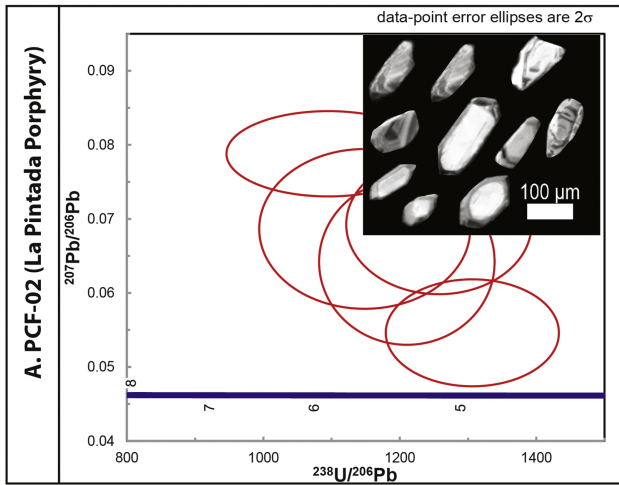


Figure 5

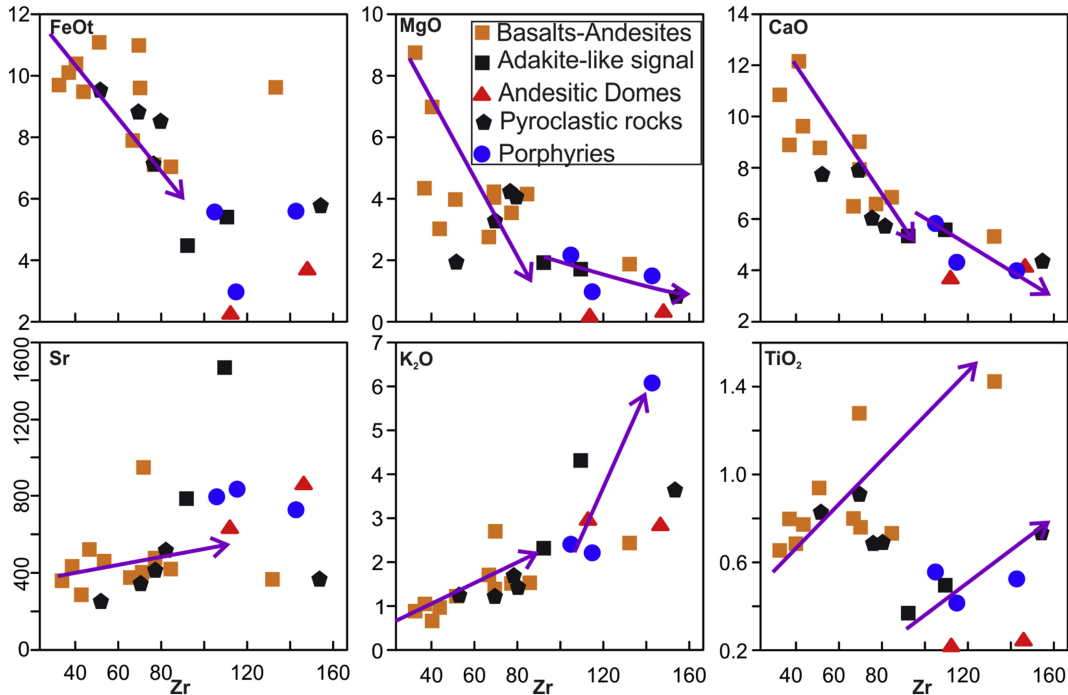


Figure 6

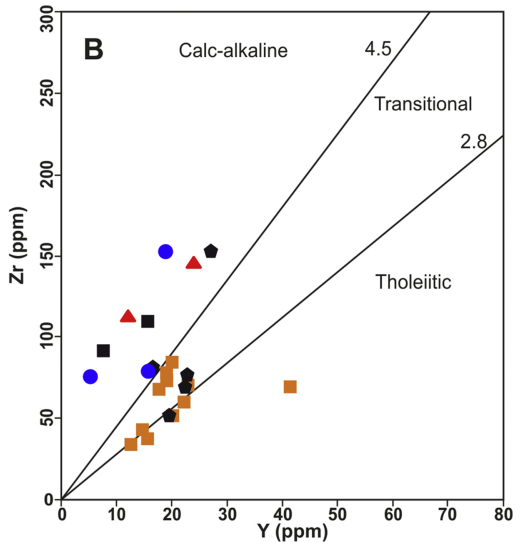
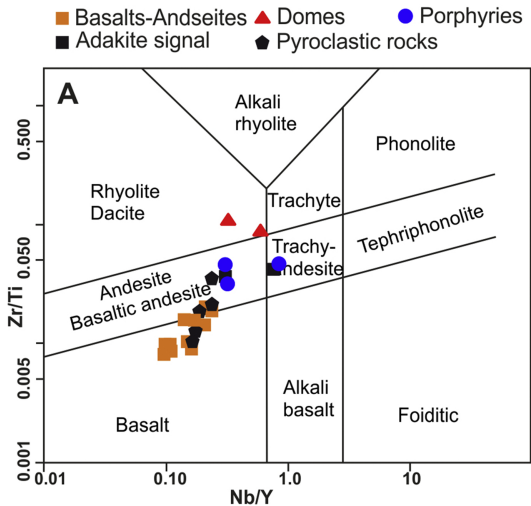


Figure 7

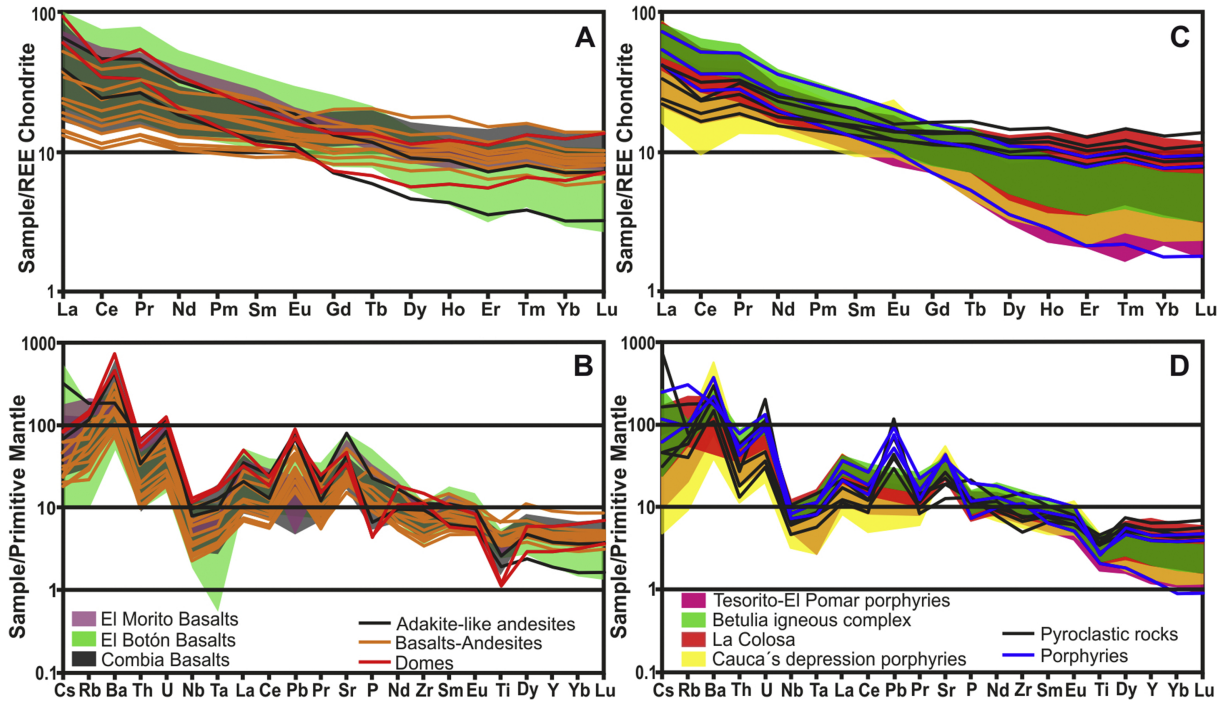


Figure 8

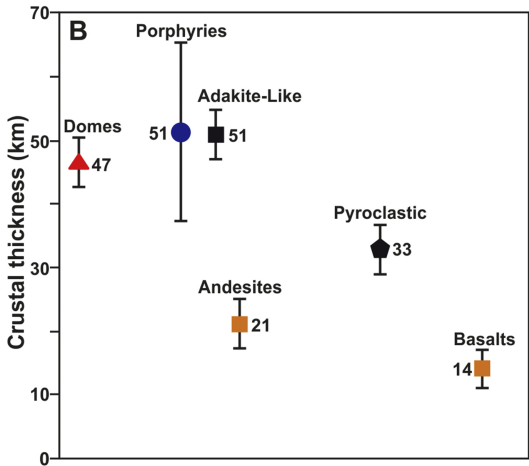
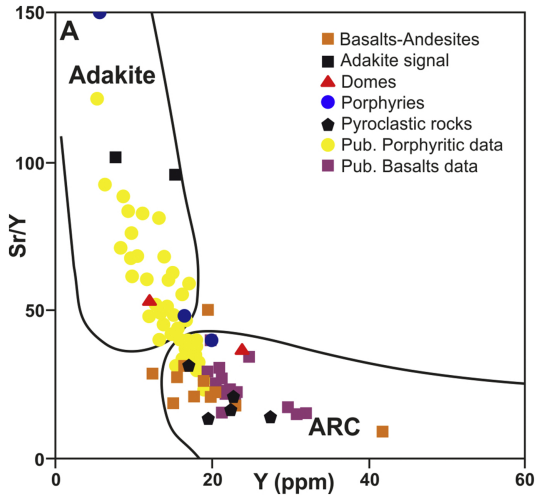


Figure 9

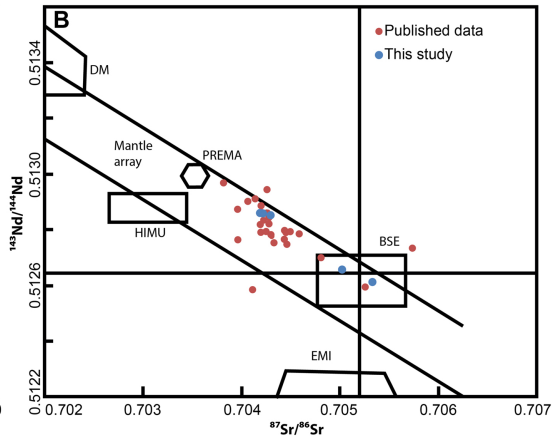
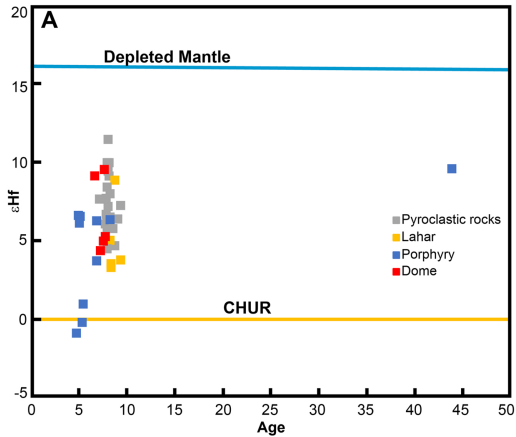


Figure 10

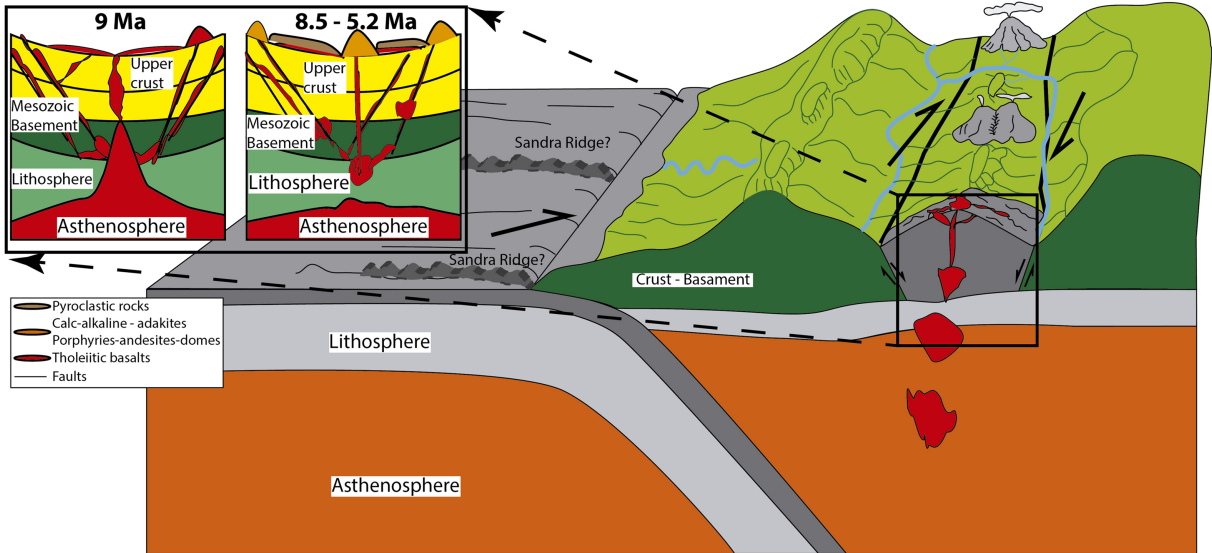


Figure 11